

Inhibition of ATM reverses radioiodine resistance in differentiated thyroid cancer via genotoxic stress amplification

Received: 9 January 2026

Accepted: 19 April 2026

Published online: 27 April 2026

Cite this article as: Qiu X., Zhao L., Jiang Y. *et al.* Inhibition of ATM reverses radioiodine resistance in differentiated thyroid cancer via genotoxic stress amplification. *J Transl Med* (2026). <https://doi.org/10.1186/s12967-026-08190-2>

Xiaotong Qiu, Li Zhao, Yongji Jiang, Simin Liu, Zhongwei Lv, Chuanzi Zuo, Yanlei Huo, Ru Wang, Yichuan Pang & Chao Ma

We are providing an unedited version of this manuscript to give early access to its findings. Before final publication, the manuscript will undergo further editing. Please note there may be errors present which affect the content, and all legal disclaimers apply.

If this paper is publishing under a Transparent Peer Review model then Peer Review reports will publish with the final article.

Title Page**Title:**

**Inhibition of ATM Reverses Radioiodine Resistance in Differentiated
Thyroid Cancer via Genotoxic Stress Amplification**

Authors:

Xiaotong Qiu^{1†}, Li Zhao², Yongji Jiang^{1†}, Simin Liu^{1†}, Zhongwei Lv^{1,3}, Chuanzi Zuo¹,
Yanlei Huo¹, Ru Wang¹, Yichuan Pang^{1*} and Chao Ma^{1*}

Affiliations:

¹ Department of Nuclear Medicine, Shanghai Tenth People's Hospital, Tongji
University School of Medicine, Shanghai, China

² The Affiliated Qingdao Central Hospital, Qingdao University, Nuclear Medicine
Imaging Department, Shandong Qingdao, China

³ Shanghai Public Health Clinical Center, Fudan University, Shanghai, China

† These authors share first authorship.

Corresponding Author:

Dr. Chao Ma

Department of Nuclear Medicine,
Shanghai Tenth People's Hospital,
Tongji University School of Medicine,
301 Yanchang Road,
Shanghai, China, 200072

Email: mc_7419@hotmail.com.

<https://orcid.org/0000-0002-1105-6793>.

Tel.: +86-187-2128-8964

Fax: +86-21-6598-3358

Reprint requests should be directed to Dr. Chao Ma.

ARTICLE IN PRESS

Abstract

Background: Radioiodine (RAI) resistance is a major barrier in the treatment of differentiated thyroid cancer (DTC), especially in tumors that retain iodine uptake but fail to respond. The role of DNA repair mechanisms, particularly ataxia-telangiectasia mutated (ATM) kinase, in this resistance remains unclear.

Methods: Single-cell RNA sequencing (scRNA-seq) was performed on 28 thyroid cancer (TC)/adjacent normal tissues to trace ATM expression during tumor dedifferentiation using publicly available datasets. Tissue microarrays from 89 TC/adjacent normal tissues cases, including RAI-avid and RAI-refractory (RAIR) tumors, validated ATM expression patterns. Therapeutic synergy between the ATM inhibitor AZD1390 and RAI was evaluated in xenograft models and K1 thyroid cancer cells. Mechanistic studies included RNA sequencing, comet assays, cell cycle profiling, and apurinic/apyrimidinic (AP) site quantification.

Results: scRNA-seq revealed stepwise ATM upregulation during TC progression, accompanied by cell cycle dysregulation. TMA analysis confirmed significantly higher ATM expression in anaplastic thyroid cancer and RAIR tumors (median score: 21.82 vs. 4.85 in RAI-sensitive; $P < 0.0001$). AZD1390 combined with RAI significantly suppressed tumor growth and enhanced apoptosis ($P < 0.001$). Mechanistically, radioiodine exposure was associated with prominent oxidative base damage-related DNA lesions, including AP sites, whereas canonical markers of extensive and persistent double-strand break accumulation were not prominently detected under these experimental conditions. ATM inhibition did not

markedly increase the initial burden of radioiodine-induced DNA lesions but impaired cell cycle checkpoint control, promoting the conversion of sublethal AP site-associated damage into lethal genomic instability.

Conclusion: ATM promotes RAI resistance by enabling repair of AP sites and enforcing cell cycle arrest. Its inhibition converts sublethal lesions into cytotoxic damage and restores RAI sensitivity, highlighting ATM as a promising therapeutic target in RAI-refractory DTC. Further studies are required to evaluate long-term safety and durability of therapeutic response.

Keywords: Thyroid cancer, radioiodine resistance, ATM, targeted therapy, base excision repair

Introduction

Differentiated thyroid cancer (DTC), accounting for 90-95% of thyroid malignancies[1], typically carries a favorable prognosis following standard therapies, including surgery, radioactive iodine (RAI), and thyroid-stimulating hormone suppression[2]. However, 5-20% of patients experience recurrence or metastasis within 20-25 years, and 10-15% develop distant metastases[3, 4]. For these metastatic cases, RAI remains a cornerstone treatment. Yet its efficacy is hampered by two intertwined challenges: dose-limiting toxicity and RAI resistance, particularly in metastases that retain iodine uptake capacity (e.g., bone metastases) but evade apoptosis, a phenomenon termed RAI-refractory (RAI-R) DTC[3]. RAI-R-DTC patients face dismal outcomes, with a median survival of 3-5 years[5], underscoring the urgent need to unravel resistance mechanisms. The

2016 ATA guidelines 3 define four RAI-R categories, from lesions with no uptake to those that retain uptake but do not respond[3]. In this study we focus specifically on the ATA category characterized by measurable ^{131}I uptake but failure to achieve a clinical response (i.e., lesions that take up radioiodine yet remain refractory), because the therapeutic strategy of impairing DNA repair to potentiate ^{131}I cytotoxicity is most relevant to tumors that receive radioactive iodide but fail to undergo cell death.

RAI exerts cytotoxicity primarily through ionizing radiation-induced DNA damage, classically attributed to DNA double-strand breaks (DSBs)[6]. Unlike external beam radiotherapy, RAI efficacy relies on functional sodium/iodide symporter (NIS)-mediated uptake, a process frequently impaired in advanced disease[7]. Nevertheless, approximately 47% of metastatic DTCs retain NIS expression but remain RAI-resistant[4], suggesting that resistance involves factors beyond iodine transport.

One critical, yet underexplored, contributor is the DNA damage response (DDR). RAI-induced DSBs activate the apical DDR kinase ataxia-telangiectasia mutated (ATM), which regulates cell cycle arrest, DNA repair, and apoptosis[8-10]. Paradoxically, excessive DDR activation may promote tumor survival by enabling DSB repair and disrupting apoptosis[11]. This duality is mirrored in clinical observations: cells from Ataxia Telangiectasia (A-T) patients (lacking functional ATM) exhibit radiosensitivity due to defective DSB repair[12], and ATM inhibition

in thyroid cancer cells has been shown to restore NIS function and enhance RAI uptake and cytotoxicity[13].

While NIS downregulation remains the primary focus in RAI-R research, the role of DDR, particularly ATM signaling, is less understood. Notably, ATM not only orchestrates DSB repair but also influences NIS expression[13], linking DDR directly to RAI responsiveness. Although ATM inhibitors have been evaluated in combination with external radiation across various tumor types[14, 15], their interaction with internal radiation modalities like RAI has not been systematically studied.

Here, we investigate the role of ATM in DTC progression and RAI resistance. We assess ATM expression across thyroid cancer stages and evaluate whether ATM inhibition can sensitize DTC cells to RAI both in vitro and in vivo. Our study aims to provide mechanistic insights into how ATM activity may promote resistance to RAI and to explore its potential as a therapeutic target in RAI-R-DTC.

Materials and Methods

Single-Cell RNA Sequencing Analysis

The GSE193581 dataset was analyzed with R/Seurat, including SCTransform normalization, UMAP, and clustering. Following the workflow described by Lu et al.[16], quality control and normalization were conducted using the Seurat package (v4.0.5). Low-quality cells with fewer than 200 genes, more than 6,000 genes, or mitochondrial gene expression exceeding 30% were excluded. Gene

expression counts were normalized using Seurat's SCTransform method, and highly variable genes were identified for downstream analysis. Dimensionality reduction was performed using UMAP, and clustering was conducted using the Louvain algorithm with a resolution of 0.5.

Cell clusters were annotated based on known marker genes, manual curation, and predictions from the modeling tool described in Lu et al[16]. Major cell types included: Epithelial cells (normal and malignant): *EPCAM*, *KRT18*, *KRT8*, *TFF3*, *TPO*, and *SLC26A4*. Fibroblasts: *COL1A1*, *DCN*, *PDPN*. Endothelial cells: *PECAM1*, *VWF*, *CDH5*. B cells: *CD79A*, *MS4A1*. T cells: *CD3E*, *CD4*, *CD8A*. NK cells: *NKG7*, *GNLY*, *KLRD1*. Myeloid cells: *CD14*, *LYZ*, *ITGAM*. Malignant epithelial cells were identified using the scTypeTC modeling tool described in Lu et al[16]. This tool integrates transcriptional signatures and machine learning to delineate tumor cell subtypes. The modeling predicted malignant cells based on the loss of thyroid differentiation markers (*TPO*, *SLC26A4*) and the expression of tumor-specific markers (*EPCAM*, *KRT18*, *KRT8*) in epithelial clusters. Both *TPO* and *SLC26A4* were absent in malignant cells, consistent with dedifferentiation during tumor progression. Malignant epithelial cells were further classified into PTC and ATC subtypes: PTC cells: Expressed epithelial markers (*KRT18*, *KRT8*) with mild dedifferentiation. ATC cells: Exhibited mesenchymal and inflammatory phenotypes, with markers such as *VCAN*, *ZEB2*, and *S100A9*.

Pseudotime trajectory analysis was performed using Monocle3 to reconstruct the transcriptional progression from normal thyroid follicular cells (NORMs) to

malignant subtypes, following the methodology outlined by Lu et al[16]. Epithelial cells (TFCs, PTC, iATC, and mATC) were selected for trajectory inference. Dimensionality reduction was performed using UMAP embeddings, and the "learn_graph" function in Monocle3 was used to infer developmental trajectories. The starting point of the trajectory was manually set to normal TFCs based on the expression of thyroid-specific markers (*TFF3*, *TPO*, *SLC26A4*). Pathway enrichment analysis was conducted using KEGG to identify pathways enriched along the pseudotime trajectory. Differentially expressed genes (DEGs) associated with cell cycle regulation were identified using Seurat's "FindMarkers" function, with a Wilcoxon rank-sum test applied to compare malignant and normal epithelial cells. Gene expression values were log2-transformed and z-score normalized across samples. The heatmap was generated using the ComplexHeatmap package in R, with hierarchical clustering used to group genes and cell types.

Tissue Microarray and Immunohistochemistry

An 89-sample tissue microarray from Shanghai Tenth People's Hospital, comprising normal, cancerous, and metastatic thyroid tissues, was used. All samples were obtained with patient consent.

Human sample information

Human samples (normal thyroid, TC, paraneoplastic, and metastatic tissues specimens) were obtained with the patient's consent through the Shanghai Tenth People's Hospital. This study was approved by the Institutional Review Board of Shanghai Tenth People's Hospital (approval number: 24KN265). To identify the

expression of ATM in TCs, a tissue microarray (TMA) was constructed, including 89 samples, including normal thyroid tissues, thyroid cancer (TC) tissues, paraneoplastic tissues, and metastatic lymph nodes (2 mm tissue core per sample). All tissue samples were fixed in formalin and embedded in paraffin for IHC. Samples were dewaxed with xylene and then rehydrated in anhydrous ethanol solution. Sections were then incubated overnight at 4°C with an anti-ATM antibody (1:100; #2873T, CST) and followed by incubation with the secondary antibody. Two independent pathologists assessed the positivity and staining intensity of the tissue sections blindly.

The expression levels were assessed based on the staining intensity (0 for no staining, 1 for weak staining, 2 for moderate staining, and 3 for strong staining) and the positive cell ratio (0 for < 10%, 1 for 10 to < 50%, and 2 for \geq 50% cell). The histochemistry score (H-SCORE) was calculated as follows: H-SCORE = (percentage of cells with weak staining \times 1) + (percentage of cells with medium staining \times 2) + (percentage of cells with strong staining \times 3).

TIMER2.0 Database Analysis

To enhance the understanding of the role of ATM in thyroid cancer, the Cancer exploration module from the TIMER2.0 database was utilized to investigate the correlation between ATM expression and the expression levels of genes associated with thyroid cancer dedifferentiation. The Gene_Corr module analyzes the relationship between ATM expression and the *BRAF*, *KRAS*, *MTOR*, and *PIK3CA* gene expression. A correlation coefficient of $0.1 \leq \rho \leq 1.0$ indicates a significant

correlation between ATM and thyroid cancer dedifferentiation genes, while a $p < 0.05$ denotes statistical significance.

Cell Culture and Treatments

The K1 (RRID: CVCL_2537), BCPAP (RRID: CVCL_0153), and TPC-1 (RRID: CVCL_6298) cell lines were procured from the American Type Culture Collection (ATCC, Manassas, VA, USA). K1 cells were incubated in medium DMEM (Gibco) supplemented with 1% Penicillin-Streptomycin solution (100x Gibco) and 10% FBS (Avantor). The cells were maintained at 37 °C in 5% CO₂. BCPAP and TPC-1 cells were incubated in medium RPMI-1640 (Gibco) supplemented with 1% Penicillin-Streptomycin solution (100x Gibco), and 10% FBS (Avantor). The cells were maintained at 37 °C in 5% CO₂. Treatments included AZD1390 (5–50 nM) and ¹³¹I (0.74–4.6 MBq/mL), alone or combined.

Radioiodine Uptake Assay

K1, BCBAP, and TPC-1 cells were seeded into 12-well plates at a density of 5×10^5 cells per well separately, with three replicate wells prepared for each cell line. Each well was supplemented with 1 mL of complete medium and incubated at 37° C in a 5% CO₂ atmosphere for 24 hours. For ATM inhibition, cells were pretreated with AZD1390 for 6–12 h prior to radioiodine exposure to ensure effective suppression of ATM activity. Following pretreatment, cells were incubated with 1 mL of serum-free medium containing 0.74 MBq ¹³¹I and 5 μM potassium iodide (KI) for 1 h at 37 °C. KI was included at a low concentration to provide a physiological iodide background; this concentration is substantially below the

threshold required to induce the Wolff-Chaikoff effect or competitively inhibit sodium/iodide symporter (NIS)-mediated iodide uptake. After incubation, the medium was aspirated and collected as the supernatant fraction. Cells were washed twice with 400 μ L of ice-cold phosphate-buffered saline (PBS), and the wash fractions were collected. Cells were then trypsinized and lysed with 0.33 M NaOH containing 1% SDS to obtain the cellular fraction. Radioactivity in both the supernatant and cellular fractions was measured using a γ -counter (GC-1200). For uptake analysis, only the radioactivity associated with the cellular fraction was used. To account for differences in cell number, uptake values were normalized to 1×10^5 viable cells based on cell counts obtained from parallel wells. Subsequently, the three replicate wells were incubated with 1 mL of serum-free medium containing 5 μ M potassium iodide (KI) and 0.74 MBq ^{131}I for 1 hour at 37°C in a 5% CO₂ atmosphere. Subsequently, the radioactive medium was aspirated from the supernatants of 12-well plates. To wash the cells, 400 μ L of pre-cooled phosphate-buffered saline (PBS) at 4 °C was added and repeated twice. The aspirated medium and PBS were collected. Cells in each well were then digested with 200 μ L of 0.25% trypsin at room temperature. The digestion was terminated by adding 500 μ L of NaOH containing 1% SDS (0.33 M) to lyse the cells, which were collected upon completion of the lysis process. Following collection, the cells were rinsed twice by adding phosphate-buffered saline (PBS) to the wells. The rinsed PBS was subsequently collected. The radioactivity in the supernatant and the lysed cells was measured using a γ -counter (GC-1200).

In Vivo Tumor Models

SPF nude BALB/c female mice (4-6 weeks old, weighing approximately 20 g) were purchased from Shanghai SLAC Laboratory Animal Co., Ltd., China, and placed in the SPF facility of the Tenth People's Hospital, Tongji University School of Medicine. To improve RAI uptake in mouse tumors, thyroid tissues in mice were removed by electroacupuncture before tumor cell injection. Postoperatively, they were given a normal diet of 0.1% calcium gluconate (to prevent calcium deficiency due to intra-operative parathyroid damage) to feed. Levothyroxine was also supplemented, and L-T4 at a dose of 14ug/Kg BW was given daily by gavage to prevent hypothyroidism until 7 days before treatment with RAI. Shanghai Tenth People Hospital's Animal Ethics Committee approved these experiments according to the Guidelines for the Care and Use of Laboratory Animals (approval number: SHDSYY-2024-4456).

Xenograft tumors in nude mice: K1 cells (1×10^6) were implanted into mice through hypodermic injection, the mice were randomized into four groups (n=7): vehicle (intraperitoneal injection of 100uL saline), RAI (a single intraperitoneal injection of 37 MBq of ^{131}I solution per mice once), iATM (per mice was injected intraperitoneally with 5mg/kg AZD1390 QD for 12 days), RAI + iATM (a single intraperitoneal injection of 37 MBq of ^{131}I solution once and intraperitoneal 5mg/Kg AZD1390 QD per mice for 12 days). These mice were housed in a clean barrier system at 20-25°C and 50-60% humidity, with free access to food and water. Tumor growth was monitored by digital calipers every 3 days, and tumor volumes

were recorded using the following formula: Volume = (longer diameter × shorter diameter²)/2. All mice were executed on day 12. AZD1390 was selected for this study due to its high potency and selectivity as an ATP-competitive ATM kinase inhibitor, as well as its favorable pharmacokinetic properties. Notably, AZD1390 has demonstrated promising radiosensitizing effects and a manageable safety profile in early-phase clinical studies [17, 18], supporting its translational relevance. The dosing regimen of AZD1390 (5 mg/kg, once daily) was determined based on previously published preclinical studies evaluating ATM inhibition as a radiosensitization strategy, as well as preliminary optimization experiments in our model to ensure tolerability and effective pathway inhibition. This regimen was selected to achieve sufficient suppression of ATM signaling while minimizing systemic toxicity.

Histological analyses of the mice's tumors: Tumor tissues were fixed in 10% formalin at room temperature, dehydrated with graded ethanol and xylene, and embedded in paraffin. Paraffin-embedded tissues were sectioned at a thickness of 5 µm. Sections were stained with hematoxylin and eosin (H&E), Ki-67, and TUNEL according to standard protocols. For immunohistochemical staining of γH2AX, sections were deparaffinized and rehydrated, followed by heat-induced antigen retrieval in 1 mmol/L Tris-EDTA buffer (pH 9.0). Slides were placed in boiling antigen retrieval buffer for 15 min, maintained at this temperature for an additional 15 min, and then allowed to cool naturally to room temperature. Endogenous peroxidase activity was blocked with hydrogen peroxide. Sections

were incubated with anti- γ H2AX antibody (1:200, #NB100-638, Novus Biologicals) overnight at 4 °C, followed by HRP-conjugated secondary antibody using the EnVision detection system. Signals were visualized using diaminobenzidine (DAB) and counterstained with hematoxylin. Slides were scanned using a digital pathology slide scanner (KFBIO), and the percentage of γ H2AX-positive staining was quantified using ImageJ software.

Liver and Renal Function Assessment: Liver and renal function were evaluated by measuring serum levels of alanine aminotransferase (ALT), aspartate aminotransferase (AST), alkaline phosphatase (ALP), blood urea nitrogen (BUN), and creatinine (CR). Blood samples were collected and allowed to clot at room temperature for 2 hours or at 4°C overnight, followed by centrifugation at 3000 rpm for 15 minutes at 2-8°C to obtain serum. The supernatant was either analyzed immediately or aliquoted and stored at -20°C or -80°C until use, avoiding repeated freeze-thaw cycles. Prior to analysis, thawed samples were re-centrifuged to remove debris. Biochemical measurements were performed using a fully automated biochemical analyzer (GH-100, Servicebio, China). All samples were analyzed in accordance with standardized protocols, and measurements were conducted under consistent experimental conditions.

Functional Assays

CCK-8: Cell viability was examined using the Cell Counting Kit-8 (CCK-8) (#GK10001, GLPBIO) assay. The cells were plated in 96-well plates (about 5×10^3 cells/well in 100 μ L culture medium) and incubated for 48h. Then we replaced the

medium with 0-1500uCi/mL concentration of ^{131}I (adding 5nM KI per well) or 0-300uM AZD1390 2.3 MBq/mL ^{131}I + 0-300nM AZD1390 (adding 5nM KI per well). After maintaining 48h or 96h, the CCK-8 working solutions were added. Then the cells were incubated continuously for 2h at 37°C. Next, a microplate reader (Tecan, Infinite 200Pro) was used to detect each group's light absorption values at 450nm. Cell survival could be displayed by the ratio of absorption values, with the calculation formula of: (dosing-blank) / (control-blank).

The synergistic effect of RAI and ATM inhibitor was demonstrated through isohologram analysis. The CompuSyn software generates a CI value to quantify the interactions between drugs[19]. This CI value was calculated following the methodology outlined by Chou et al.[20, 21]. A CI value approaching 1 suggests additive effects of the drug combinations, while values less than 1 indicate synergy, and values greater than 1 indicate antagonism.

Colony Formation: Cells were plated in T25 culture bottles at 1.0×10^3 cells per bottle in medium DMEM supplemented with 100 units/mL penicillin + 100 mg/mL streptomycin, and 10% FBS and incubated at 37°C in 5% CO_2 for 7 days. Then these cultured cells were divided into a control group, a ^{131}I -irradiated group, an ATM inhibitor group, and a combined ^{131}I and ATM inhibitor group. The control group was untreated, 2.3 MBq/mL ^{131}I and 5nM KI were added to the ^{131}I group, and 5nM or 10nM AZD1390 were added to the ATM inhibitor group; the combined group was treated by the addition of 2.3 MBq/mL ^{131}I + 5nM KI + 5nM (or 10nM) AZD1390. The culture medium was changed every 3 days. After another 7 days,

cells were fixed in 4% PFA for 10 min at room temperature and stained with 0.1% crystal violet for 10 min at room temperature, following 3 washes with water, air-dried, and photographed.

Apoptosis / Cell Cycle: The apoptosis detection was performed using the Annexin V-FITC/PI apoptosis kit (#AP101, MultiSciences). Flow cytometry was run using a BD Fortessa flow cytometer (BD Biosciences), and data were analyzed using FlowJo 10.8.1. software (FlowJo LLC). Each program was conducted 3 times. The cell cycle detection was performed using the Cell Cycle Staining Kit (MultiSciences, CCS012). Flow cytometry was run using a BD Fortessa flow cytometer (BD Biosciences), and cell populations in G1, S, and G2/M, were measured using FlowJo 10.8.1. software (FlowJo LLC). Each program was conducted 3 times.

Comet assay: For the Comet assay (KeyGEN, China), cells were embedded in 0.7% low-melting-point agarose and subjected to alkaline lysis. Alkaline DNA unwinding was performed in a buffer containing 300 mM NaOH and 1 mM EDTA (pH > 13) for 40 minutes at room temperature. Electrophoresis was then conducted at 25 V for 30 minutes. After neutralization and staining with Propidium Iodide (PI), 50 randomly selected cells per sample were imaged using a fluorescence microscope (515-560 nm). DNA damage was quantified by measuring the Comet Tail Length using ImageJ software.

AP site assay (Dojindo, Japan): genomic DNA was extracted and normalized to a precise concentration of 100 µg/mL in TE buffer. AP sites were labeled with an Aldehyde Reactive Probe (ARP) for 1 hour at 37 °C. Following purification via

filtration tubes, the ARP-labeled DNA was immobilized on a 96-well plate and detected using HRP-Streptavidin. The absorbance was measured at 650 nm, and the number of AP sites per 10^5 bp was calculated against a standard curve ranging from 0 to 40 sites.

5-Ethynyl-2'-deoxyuridine (EdU) proliferation assay: Cell proliferation was detected using the EdU cell proliferation assay according to the manufacturer's instructions (#C0071S, Beyotime). Around 3×10^4 K1 cells were plated into glass-bottomed dishes (#800102, NEST) and kept for 48h. Cells were collected at the indicated times after treatment with or without ^{131}I irradiation. Confocal microscopy was conducted using a Zeiss LSM900 microscope with a 60x oil-immersion lens following standard protocol, and images were analyzed using ImageJ software.

TUNEL: Terminal deoxynucleotidyl transferase (TdT)-mediated FITC-12-dUTP nick end labeling (TUNEL) using TUNEL Fluorescent In Situ Apoptosis Detection Kit (#40306ES20, Yeasen), according to the manufacturer's instructions. Around 3×10^4 cells were plated into glass-bottomed dishes (#800102, NEST) and kept for 48h before the assay. Cells were collected at the indicated times after treatment with or without RAI irradiation. Confocal microscopy was conducted using a Zeiss LSM900 microscope with a 60x oil-immersion lens following standard protocol, and images were analyzed using ImageJ software.

Immunofluorescence staining of dsDNA and ssDNA: Cells were collected at the indicated times to detect cytosolic DNA in K1 cells after RAI irradiation. K1

cells were fixed with 4% PFA and permeated with 5% Triton X-100. Then blocked with 1% BSA in PBS, and incubated with anti-dsDNA (1:400; #MAB1293, AE2, Millipore) or anti-ssDNA (1:400, # MAB3299, F7-26, Millipore) primary antibody overnight at 4°C. After 3 washes with PBS, the cells were incubated with donkey anti-mouse-Alexa Fluor 555 (#A-31570, Thermo Fisher) for 1h at room temperature. Subsequently, DAPI staining was performed at room temperature for 10 min. Confocal microscopy was conducted using a Zeiss LSM900 microscope with a 60x oil-immersion lens following standard protocol, and images were analyzed using Image J software.

Molecular Analyses

RNA-seq: RNA sequencing data have been deposited in the GEO database under accession number GSE297164. Libraries were sequenced on the NovaSeq X Plus platform (PE150) using the NovaSeq Reagent Kit. Raw paired-end reads were quality filtered and trimmed using fastp[22] with default parameters. Clean reads were aligned to the reference genome using HISAT2[23] in orientation mode. Transcript assembly was performed using StringTie[24] in a reference-based approach. Gene expression quantification was performed using RSEM[25], which generated both raw read counts and transcripts per million (TPM) values. Raw gene-level count matrices were used as input for differential expression analysis with DESeq2[26]. TPM values were used for visualization and expression level comparisons. Differentially expressed genes (DEGs) were defined using a threshold of $|\log_2 \text{fold change}| \geq 1.3$ and false discovery rate (FDR) < 0.05 .

DEGseq[27].was also used as a complementary method with an FDR threshold < 0.001. Functional enrichment analysis including Gene Ontology (GO) and KEGG pathway analysis was performed using Goatools and Python SciPy, respectively, with Bonferroni-corrected $P < 0.05$ considered significant. Gene set enrichment analysis (GSEA) was performed to evaluate pathway-level expression changes.

Western Blot: Cells were seeded in six-well plates at a density of 50% and incubated at 37°C for 24 hours. Cells were divided into four groups: Control, RAI (treated with 2.3 MBq/mL ^{131}I), iATM (treated with 50nM AZD1390), ^{131}I + iATM (treated with 2.3 MBq/mL ^{131}I + 50nM AZD1390). Proteins were harvested after 24 hours of the above treatment by scraping the cells in radioimmunoprecipitation assay (RIPA) lysis buffer supplemented with a protease inhibitor cocktail (#K1007, APExBIO). Protein content was quantified using the BCA Protein Assay Kit according to the manufacturer's instructions (#T9300A, Takara). Standard methods of Western blot have been used to analyze each protein expression. Primary antibodies used were anti-ATM (#A19650, ABclonal), anti-Phospho-ATM-S1981 (#AP1030, ABclonal), anti-CDK1 A17 (#ab18, Abcam), anti-Phospho-CDC2 Tyr15 (#9117, CST), and anti-GAPDH (#2118, CST).

Statistical Analysis

Statistics were analyzed using GraphPad Prism 9.0 and IBM SPSS Statistics 20 software. Results were presented as mean \pm SD as indicated in the figure legends. Unpaired samples t-test, one-way or two-way ANOVA, Tukey's multiple comparison tests, ns > 0.05, * $p < 0.05$, ** $p < 0.01$, *** $p < 0.001$, **** $p < 0.0001$.

Results

Single-Cell Analysis Indicates ATM as a Driver of Thyroid Cancer Progression.

Single-cell RNA sequencing (scRNA-seq) of 28 thyroid tissue samples, including 15 anaplastic thyroid cancers (ATC), 7 papillary thyroid cancers (PTC), and 6 normal thyroid follicular epithelial cell samples delineated the trajectory of malignant progression[28]. Uniform Manifold Approximation and Projection (UMAP) revealed eight distinct cell populations[28], including epithelial, immune subsets, fibroblasts, endothelial cells (Fig. 1A, S1A-B), validated by marker gene profiling (*KRT18* for epithelium, *PECAM1* for endothelium) (Fig. 1B).

To visualize the dynamic transcriptional evolution of epithelial cells, we reconstructed a pseudotime developmental trajectory using Monocle3 (Fig. 1C & Fig. S1C). This trajectory clearly revealed a gradual transition from normal thyroid follicular cells (NORM) through PTC to ATC, indicating a continuous dedifferentiation process during tumor evolution. KEGG pathway enrichment along this trajectory revealed a stepwise activation of metabolic (e.g., ribosome biogenesis, oxidative phosphorylation) and oncogenic signaling pathways (e.g., PI3K-Akt, relaxin) (Fig. S1D). A comparative analysis highlighted the ATC-specific upregulation of cell cycle (adjusted $P < 0.05$) and chromosomal instability genes (*BUB1*, *MCM2*) compared to NORM (Fig. 1D-E). Critically, among cell cycle-associated genes, ATM was identified as progressively upregulated during

dedifferentiation (Fig. 1F), implicating it as a potential driver of genomic instability and aggressive tumor progression.

Clinical Validation of ATM Overexpression in Advanced and RAI-Resistant Thyroid Cancer.

We validated ATM's clinical relevance via immunohistochemistry on 89 thyroid samples, including normal thyroid tissues, primary tumors, adjacent tissues, and metastatic lymph nodes (Fig. S2A-B and Supplemental Table 1). Consistent with scRNA-seq data, ATM protein levels were significantly elevated in thyroid cancer tissues compared to adjacent normal tissues ($p < 0.05$) (Fig. 2A). ATM expression was highest in ATC tissues, significantly exceeding levels in PTC and follicular thyroid carcinoma (FTC) samples ($P < 0.0001$) (Fig. 2B).

In RAI-refractory (RAI-R) PTC, ATM expression was substantially elevated, with a median score of 21.82 (95% CI: 12.59-29.20), compared to radioiodine-avid (RIA) PTC cases (median score 4.85, 95% CI: 3.17-12.99) and normal paraneoplastic tissues (median score 2.89, 95% CI: 1.31-8.44) (Fig. 2C). Metastatic lymph nodes from RAI-R PTC cases exhibited higher ATM scores (median 7.20, 95% CI: 5.60-16.60) compared to those from RIA cases (median 2.33, 95% CI: 0.73-13.84) (Fig. 2D). Correlation analysis using the TIMER2.0 database revealed positive associations between *ATM* and oncogenic drivers including *BRAF* ($\rho = 0.546$), *KRAS* ($\rho = 0.636$), *MTOR* ($\rho = 0.546$), and *PIK3CA* ($\rho = 0.704$) (Fig. 2E). Figure 2F presents representative images of ATM staining for different tissue types.

Targeting ATM Inhibition Synergizes with RAI to Suppress Tumor Growth In Vivo.

To evaluate ATM inhibition in vivo, we evaluated multiple thyroid cancer cell lines available in our laboratory, including BCPAP, K1, and TPC-1, among the tested cell lines, K1 exhibited moderate but detectable ^{131}I uptake, representing a suitable model of partial radioiodine refractoriness (Fig. S3A). As baseline ATM expression did not differ significantly across tested cell lines (Fig. S3B). Having established this model, we next ensured that the ATM inhibitor AZD1390 itself did not interfere with the fundamental mechanism of RAI action. AZD1390 treatment did not significantly alter radioiodine uptake at 6 h or 12 h, suggesting that ATM inhibition does not affect iodide transport in thyroid cancer cells (Fig. S3C).

Tumor-bearing nude mice were treated with RAI (37 MBq, single dose), the ATM inhibitor AZD1390 (5 mg/kg, daily), or the combination for 12 days (Fig. 3A, B). Tumor volumes were significantly reduced in the combination group compared to monotherapies ($P < 0.01$, two-way ANOVA) (Fig. 3C). Final tumor weights were also significantly lower in the combination group.

Immunohistochemistry analysis of excised tumors showed decreased Ki-67 staining and increased TUNEL staining in the combination group ($P < 0.001$) (Fig. 3D-E). While ^{131}I alone activated the DDR, evidenced by γH2AX foci accumulation, co-treatment with AZD1390 suppressed γH2AX levels, indicating compromised DDR signaling (Fig. 3D-E). These findings suggest that ATM inhibition potentiates

RAI efficacy by impairing DNA repair and promoting apoptosis. To evaluate potential systemic toxicity associated with ATM inhibition combined with radioiodine therapy, serum biochemical parameters were analyzed in treated mice. No significant differences were observed in liver function markers (ALT, Alanine Aminotransferase, AST, Aspartate Aminotransferase, ALP, Alkaline phosphatase) or renal function markers (BUN, Blood Urea Nitrogen, CR, Creatinine) between treatment groups, indicating that the combination therapy did not induce detectable hepatic or renal toxicity under the experimental conditions used (Fig. 3F). However, hematologic toxicity, particularly bone marrow suppression, was not evaluated in this study and remains an important consideration for future investigation.

ATM Blockade Potentiates RAI-Induced Cytotoxicity and Suppresses Migration In Vitro.

In vitro, ATM inhibition radiosensitized K1 cells treated with ^{131}I (0–55.5 MBq/mL) or AZD1390 (0–1200 nM) for 48–92 hours. CCK-8 assays revealed time- and dose-dependent inhibition of cell proliferation by ^{131}I , while AZD1390 alone showed minimal cytotoxicity (Fig. 4A-B). Co-treatment with ^{131}I (2.3 MBq/mL) and AZD1390 (1.2–75 nM) significantly reduced cell viability compared to monotherapies (Fig. 4C). CompuSyn analysis confirmed synergistic inhibition (combination index <1) (Fig. 4D)[29, 30]. Colony formation assays demonstrated reduced clonogenic survival with the combination therapy ($P < 0.001$), with fewer

colonies observed at higher AZD1390 doses (Fig. 4E-F). Annexin V/PI staining showed activity-dependent increases in apoptosis upon ^{131}I treatment ($P < 0.001$), which was significantly enhanced by combination therapy ($P < 0.01$) (Fig. 4G-J). We established stable ATM-knockdown K1 cells (shATM) to genetically validate on-target effects (Fig. 4K). We first assessed the impact of ATM depletion on cell migration. Wound-healing assays revealed that ATM knockdown significantly impaired the migratory capacity of K1 cells compared to the non-targeting control (shNC) ($p < 0.05$) (Fig. 4L-M). We next asked whether genetic ATM knockdown could recapitulate the chemosensitization effect observed with AZD1390. Flow cytometric analysis of Annexin V/PI staining demonstrated that ATM knockdown alone induced an increase in apoptosis ($p < 0.01$). Crucially, the combination of ATM knockdown and RAI treatment resulted in a synergistic enhancement of apoptotic cell death, significantly exceeding the effects of either single treatment ($p < 0.0001$) (Fig. S4A-B). This genetic evidence unequivocally confirms that the sensitization to RAI is an on-target effect of ATM ablation.

RAI Induces Genotoxic Stress with Limited Detectable Double-Strand Breaks in RAI-R DTC cells.

RNA-seq of RAI-treated K1 cells identified 1,144 differentially expressed genes ($|\log_2\text{FC}| > 1.3$, $\text{FDR} < 0.05$) (Fig. S5A)[31-36]. GO and KEGG analyses revealed enrichment of DNA repair, cell cycle regulation, and G1/S transition pathways (Fig. 5A, Fig. S5C). GSEA demonstrated downregulation of mitosis- and G2/M

checkpoint-related genes, alongside activation of DNA repair pathways (FDR < 0.05) (Fig. 5B).

Transcriptomic analysis revealed differential expression of numerous DNA repair genes in response to RAI. These included a modest upregulation of key components of the base excision repair (BER) pathway, such as *POLB* (Fig. 5C), which is consistent with a cellular response to RAI-induced oxidative base damage, a known source of apurinic/apyrimidinic (AP) sites. EdU staining confirmed a time-dependent decrease in proliferation after RAI (Fig. 5D, K), but TUNEL and dsDNA staining did not reveal a sustained increase in detectable double-strand breaks (Fig. 5F-I, K). Comet assays showed limited DNA fragmentation under these experimental conditions in ^{131}I -treated cells compared to DNase I controls (Fig. 5G, K). Notably, RAI induced modest increases in single-stranded DNA (ssDNA) accumulation ($P < 0.01$) (Fig. 5H-J, K). These results suggest that in K1 cells with high ATM activity, RAI-induced double-strand breaks, if present, are rapidly resolved, whereas non-DSB lesions such as AP sites may persist and constitute a dominant source of unresolved genotoxic stress.

ATM Inhibition Exacerbates Genotoxic Stress and Induces Mitotic Catastrophe.

Flow cytometry revealed that ^{131}I (2.3-4.6 MBq/mL) induced G2/M arrest in K1 cells, with dose-dependent enrichment (Fig. 6A-B, D). While ^{131}I alone caused S-phase accumulation, co-treatment with AZD1390 (50 nM) further augmented

G2/M arrest (Fig. 6C-E). Western blotting confirmed that ATM inhibition attenuated phosphorylation of checkpoint kinases (pChk2, pCDC2), suggesting dysregulated G2/M checkpoint control and premature mitotic entry. (Fig. 6F-G, Fig. S6A).

To assess DNA damage persistence, cells were irradiated with ^{131}I (4.6 MBq/mL) for 24 hours, washed to remove residual RAI, and then incubated with or without AZD1390. Co-treatment of ^{131}I -AZD1390 resulted in a time-dependent accumulation of AP sites compared with RAI alone. At the same time, cell survival was reduced, emphasizing the cytotoxic consequences of impaired DNA repair (Fig. 6H). These results support that ATM inhibition disables DDR checkpoints, driving cells with unresolved damage into mitosis, ultimately triggering mitotic catastrophe and apoptosis.

Discussion

RAI remains a cornerstone therapy for DTC[6], yet its efficacy is often limited by intrinsic or acquired resistance. Our study identifies ATM as a molecular determinant associated with disease progression and therapeutic resistance in thyroid cancer. By integrating single-cell transcriptomics, clinical TMAs, functional preclinical models and in vitro mechanistic explorations, we delineate a central role for ATM in promoting dedifferentiation, genomic instability, and escape from RAI-induced cytotoxicity.

Single-cell RNA-sequencing revealed a continuum from normal thyroid follicular

cells through papillary thyroid carcinoma (PTC) to anaplastic thyroid carcinoma (ATC), with a stepwise upregulation of ATM along this dedifferentiation trajectory. Notably, this increase was predominantly confined to epithelial tumor populations rather than stromal compartments, supporting a predominantly tumor cell-intrinsic pattern of ATM in disease progression. Pseudotemporal analysis showed progressive ATM activation during tumor evolution, coinciding with cell cycle, DNA replication, and chromosomal instability programs. These findings were validated in clinical specimens, where RAI-R tumors exhibited significantly higher ATM levels than RAI-sensitive counterparts. ATM expression positively correlated with oncogenic drivers (*BRAF*, *KRAS*, *PIK3CA*[37]), suggesting a potential association with pro-tumorigenic signaling networks. While these observations strongly associate ATM upregulation with dedifferentiation, causal relationships remain to be established. Future studies involving genetic perturbation (e.g., knockdown or overexpression) will be required to determine whether ATM directly drives this process. These findings are consistent with reports in breast and gastric cancers[38, 39], where ATM overexpression is linked to both oncogenic transformation and therapy resistance, underscoring its context-dependent roles in cancer biology[40]. In addition, ATM has been implicated in epithelial-to-mesenchymal transition and loss of differentiation markers in other malignancies, supporting a potential role in thyroid cancer dedifferentiation[41]. Nevertheless, several limitations should be considered. The relatively small size of available scRNA-seq datasets and incomplete clinical annotation of TMA cohorts,

particularly regarding prior RAI exposure, may limit the resolution of resistance-associated subpopulations and clinicopathological correlations. Future studies incorporating larger, well-annotated cohorts will be essential to further validate and extend these findings.

In preclinical models, both pharmacologic and genetic ATM suppression synergized with RAI to inhibit tumor growth, induce apoptosis, and impair migration. This consistency confirms ATM's role in RAI resistance. Mechanistically, under the experimental conditions used, RAI treatment was associated with prominent accumulation of AP sites arising from oxidative base damage, while persistent or readily detectable double-strand breaks were limited. While γ H2AX was observed post-RAI, comet assays confirmed no significant DSB induction. This observation aligns with the physical properties of ^{131}I , which is primarily a low-LET β particle emitter. Unlike high-LET radiation, the sparse ionization events produced by electrons and β particles predominantly cause localized oxidative base damage and single-strand breaks, which are significantly more frequent than immediate DSBs[42]. These lesions often manifest as non-DSB clustered DNA damages, including a high density of AP sites[43]. Our findings suggest that in the context of high ATM expression, these pervasive sublethal lesions are the primary genotoxic stress managed by the cell's repair machinery. Instead, γ H2AX likely reflects replication stress from unresolved AP sites, as persistent AP lesions stall replication forks, activating ATR and downstream DDR signaling[44]. ATM inhibition exacerbated this stress by abrogating G2/M checkpoint control (pChk

and pCDC2 downregulation), forcing cells with unrepaired AP sites into mitosis, where replication errors culminated in mitotic catastrophe. While AP sites are canonically repaired via BER, the role of ATM in this context is uncharted. Intriguingly, ATM inhibition exacerbated AP site retention, suggesting its potential involvement in BER coordination. This corroborates earlier findings indicating that ATM or its signaling intermediates govern oxidative DNA damage responses[45, 46]. And researchers have shown that ATM directly participates in BER through phosphorylation of TDP1 at Ser81, a modification that enables XRCC1-dependent recruitment of TDP1 to sites of base lesions[47]. The limited detection of SSB intermediates suggests they are either transiently repaired or AP sites are processed via long-patch BER. This aligns with studies showing that oxidative agents, such as ionizing radiation, can directly generate AP sites without requiring SSB intermediates[48, 49].

Beyond its well-established role in DSB repair, our data suggest that ATM also contributes to the cellular response to RAI-induced AP site-associated genotoxic stress, likely through regulation of BER and cell cycle checkpoint control. However, the precise molecular mechanisms by which ATM modulates BER in response to radioiodine-induced oxidative damage remain incompletely defined. Future studies are warranted to elucidate whether ATM directly regulates the recruitment and activity of key BER components at AP sites, as well as how BER dynamics are coordinated with checkpoint signaling under conditions of genotoxic stress. In parallel, although ATM is known to influence DSB repair pathway choice

between homologous recombination (HR) and non-homologous end joining (NHEJ), these pathways were not directly assessed in the present study. Therefore, we cannot exclude a contributory role of altered DSB repair pathway utilization in the observed radiosensitization. Nevertheless, given the relatively limited DSB burden observed under our experimental conditions, we propose that BER-associated processes represent the dominant mechanism. Future studies integrating functional analyses of HR/NHEJ activity with BER dynamics will be important to fully delineate the interplay between these repair pathways following ATM inhibition, particularly under conditions of higher DSB burden. Collectively, these findings support a distinct model of synthetic lethality, in which ATM inhibition exacerbates the accumulation of otherwise sublethal AP sites, ultimately triggering replication catastrophe and cell death. This mechanism differs fundamentally from classical paradigms based on DSB repair deficiency, such as PARP inhibitor sensitivity in BRCA-mutant tumors, and highlights an alternative therapeutic vulnerability driven by oxidative DNA damage overload.

From a translational perspective, our findings provide a strong rationale for combining ATM inhibition with radioiodine therapy to enhance therapeutic efficacy in radioiodine-refractory thyroid cancer. Importantly, the ATM inhibitor used in this study, AZD1390, has already entered early-phase clinical development and has demonstrated manageable safety profiles when combined with radiotherapy in patients with solid tumors. In our preclinical models, the combination of AZD1390 and radioiodine did not induce detectable systemic

toxicity, as reflected by stable liver and kidney function parameters. However, this safety evaluation is limited to short-term observations, as our *in vivo* experiments were conducted over a relatively brief treatment duration. Notably, hematologic toxicity, particularly bone marrow suppression, was not assessed in the current study and remains an important concern given the radiosensitizing mechanism of ATM inhibition. In addition, the durability of the therapeutic response following treatment cessation was not evaluated. Whether the combination of ATM inhibition and radioiodine induces sustained tumor control or only transient regression requires further investigation in longitudinal studies with extended follow-up. Furthermore, although no overt systemic toxicity was observed, the potential long-term effects of transient ATM inhibition particularly with respect to genomic stability, normal tissue homeostasis, and cumulative toxicity remain to be fully defined. Given the central role of ATM in maintaining genomic integrity, careful optimization of dosing strategies and therapeutic windows will be critical for safe clinical translation. While further validation is required, our findings support the clinical exploration of this strategy in early-phase trials designed to evaluate both safety and radiosensitizing efficacy.. Rather than functioning as a continuous treatment, this strategy is conceptually designed as a transient radiosensitization approach, in which ATM inhibition is administered during the radioiodine treatment window to amplify tumor-specific genotoxic stress.

Future clinical studies may adopt dose-escalation designs to establish safety and tolerability, followed by exploratory evaluation of therapeutic efficacy. Importantly,

such trials could explore multiple treatment paradigms, including standard radioiodine alone, radioiodine combined with ATM inhibition, or reduced-dose radioiodine combined with ATM inhibition, to determine whether radiosensitization can enhance efficacy while potentially minimizing radiation exposure. From a precision medicine perspective, appropriate patient selection will be critical. Although ATM dysregulation has been associated with tumor progression and resistance to DNA-damaging therapies across multiple malignancies, it is unlikely to function as a standalone biomarker in thyroid cancer due to its molecular heterogeneity. Instead, ATM expression may serve as a complementary biomarker when integrated with established molecular alterations, such as BRAF and TERT promoter mutations, which are associated with dedifferentiation and poor radioiodine responsiveness. Collectively, these considerations support the development of a clinically testable framework in which transient ATM inhibition enhances radioiodine efficacy in molecularly defined subgroups of patients with refractory thyroid cancer, while highlighting the need for careful evaluation of long-term safety and durability of response.

The therapeutic implication is twofold: (1) ATM upregulation may serve as a biomarker of aggressive, dedifferentiated, and RAI-resistant thyroid cancer; and (2) pharmacologic targeting of ATM may represent a precision radiosensitization strategy, particularly in molecularly defined subgroups such as tumors harboring BRAF or TERT alterations. Importantly, this approach is most applicable to tumors that retain partial iodine uptake but exhibit therapeutic resistance, rather

than those with complete loss of iodide transport.

Conclusions

In summary, this study establishes ATM as a key driver of thyroid cancer progression and a therapeutic vulnerability in RAI resistance. While its direct causal role in dedifferentiation requires further validation, our data position ATM as a critical contributor to the RAI-resistant phenotype. Our findings are most applicable to tumors that retain measurable radioiodine uptake but are clinically refractory (ATA category 4), and do not imply that ATM inhibition will restore radioiodine responsiveness in tumors that lack iodide uptake. These findings provide a strong rationale for the clinical development of ATM-targeted radiosensitization strategies and suggesting that ATM inhibition may represent a potential therapeutic strategy that warrants further investigation, particularly with respect to long-term safety and durability of response.

Acknowledgements

We thank the Department of Pathology of Shanghai Tenth People's Hospital for providing clinical samples to support this study.

Author contributions

X.T.Q.: Writing - original draft, Formal analysis, Visualization. L.Z.: Data curation, Resources, Methodology. Y.J.J.: Investigation, Validation, Writing - review & editing. S.M.L.: Software, Formal analysis, Visualization. Z.W.L.: Project

administration, Resources. C.Z.Z.: Data curation, Software, Validation. Y.L.H.: Methodology, Investigation, Writing - review & editing. R.W.: Supervision, Conceptualization. Y.C.P.: Supervision, Funding acquisition, Writing - review & editing. C.M.: Conceptualization, Project administration, Writing - review & editing.

Funding

This work was supported in part by the National Natural Science Foundation of China (Grant 82171974, 82372000).

Data Availability

The data sets produced through the current study are available from the corresponding author on reasonable request.

Declarations

Ethics approval and consent to participate

The study adhered to the principles outlined in The Declaration of Helsinki. The study involving human participants, was approved by the Institutional Review Board of Shanghai Tenth People's Hospital (approval number: 24KN265). All of mouse experiments have been approved by Shanghai Tenth People Hospital's Animal Ethics Committee according to the Guidelines for the Care and Use of Laboratory Animals (approval number: SHDSYY-2024-4456).

Consent for publication

Not applicable.

Competing interests

The authors declare that they have no competing financial or non-financial interests.

References

1. Mao Y, Xing M. Recent incidences and differential trends of thyroid cancer in the USA. *Endocr Relat Cancer*. 2016;23(4):313–22.
2. Stewart LA, Kuo JH. Advancements in the treatment of differentiated thyroid cancer. *Ther Adv Endocrinol Metab*. 2021;12:20420188211000251.
3. Haugen BR, Alexander EK, Bible KC, Doherty GM, Mandel SJ, Nikiforov YE, et al. 2015 American Thyroid Association Management Guidelines for Adult Patients with Thyroid Nodules and Differentiated Thyroid Cancer: The American Thyroid Association Guidelines Task Force on Thyroid Nodules and Differentiated Thyroid Cancer. *Thyroid*. 2016;26(1):1–133.
4. Durante C, Haddy N, Baudin E, Leboulleux S, Hartl D, Travagli JP, et al. Long-term outcome of 444 patients with distant metastases from papillary and follicular thyroid carcinoma: benefits and limits of radioiodine therapy. *J Clin Endocrinol Metab*. 2006;91(8):2892–9.
5. Fugazzola L, Elisei R, Fuhrer D, Jarzab B, Leboulleux S, Newbold K, et al. 2019 European Thyroid Association Guidelines for the Treatment and Follow-Up of Advanced Radioiodine-Refractory Thyroid Cancer. *Eur Thyroid J*. 2019;8(5):227–45.
6. De la Vieja A, Riesco-Eizaguirre G. Radio-Iodide Treatment: From Molecular Aspects to the Clinical View. *Cancers (Basel)*. 2021;13(5).
7. Liu Y, Wang J, Hu X, Pan Z, Xu T, Xu J, et al. Radioiodine therapy in advanced differentiated thyroid cancer: Resistance and overcoming strategy. *Drug Resist Updat*. 2023;68:100939.
8. Shiloh Y. ATM and related protein kinases: safeguarding genome integrity. *Nat Rev Cancer*. 2003;3(3):155–68.
9. Lavin MF. Ataxia-telangiectasia: from a rare disorder to a paradigm for cell signalling and cancer. *Nat Rev Mol Cell Biol*. 2008;9(10):759–69.
10. Derheimer FA, Kastan MB. Multiple roles of ATM in monitoring and maintaining DNA integrity. *FEBS Lett*. 2010;584(17):3675–81.
11. Branzei D, Foiani M. Regulation of DNA repair throughout the cell cycle. *Nat Rev Mol Cell Biol*. 2008;9(4):297–308.

12. Blackford AN, Jackson SP. ATM, ATR, and DNA-PK: The Trinity at the Heart of the DNA Damage Response. *Mol Cell*. 2017;66(6):801-17.
13. Lyckesvård MN, Kapoor N, Ingesson-Carlsson C, Carlsson T, Karlsson JO, Postgård P, et al. Linking loss of sodium-iodide symporter expression to DNA damage. *Exp Cell Res*. 2016;344(1):120-31.
14. Batey MA, Zhao Y, Kyle S, Richardson C, Slade A, Martin NM, et al. Preclinical evaluation of a novel ATM inhibitor, KU59403, in vitro and in vivo in p53 functional and dysfunctional models of human cancer. *Mol Cancer Ther*. 2013;12(6):959-67.
15. Durant ST, Zheng L, Wang Y, Chen K, Zhang L, Zhang T, et al. The brain-penetrant clinical ATM inhibitor AZD1390 radiosensitizes and improves survival of preclinical brain tumor models. *Sci Adv*. 2018;4(6):eaat1719.
16. Lu L, Wang JR, Henderson YC, Bai S, Yang J, Hu M, et al. Anaplastic transformation in thyroid cancer revealed by single-cell transcriptomics. *J Clin Invest*. 133(11).
17. Durant SA-O, Zheng LA-O, Wang Y, Chen K, Zhang L, Zhang T, et al. The brain-penetrant clinical ATM inhibitor AZD1390 radiosensitizes and improves survival of preclinical brain tumor models. (2375-2548 (Electronic)).
18. Wen P, Yang JT, Imber BS, Drappatz J, Jena R, Forst D, et al. CTIM-16. SAFETY AND PRELIMINARY EFFICACY OF AZD1390 + RADIATION THERAPY FOR GLIOBLASTOMA. (1522-8517 (Print)).
19. Kifer DA-O, Jakšić DA-OX, Šegvić Klarić M. Assessing the Effect of Mycotoxin Combinations: Which Mathematical Model Is (the Most) Appropriate? LID - 10.3390/toxins12030153 [doi] LID - 153. (2072-6651 (Electronic)).
20. Chou TC. Theoretical basis, experimental design, and computerized simulation of synergism and antagonism in drug combination studies. (0031-6997 (Print)).
21. Chou Tc Fau - Talalay P, Talalay P. Quantitative analysis of dose-effect relationships: the combined effects of multiple drugs or enzyme inhibitors. (0065-2571 (Print)).
22. Chen S, Zhou Y, Chen Y, Gu J. fastp: an ultra-fast all-in-one FASTQ preprocessor. (1367-4811 (Electronic)).
23. Kim D, Langmead B, Salzberg SA-O. HISAT: a fast spliced aligner with low memory requirements. (1548-7105 (Electronic)).
24. Pertea M, Pertea GM, Antonescu CM, Chang TC, Mendell JT, Salzberg SA-O. StringTie enables improved reconstruction of a transcriptome from RNA-seq reads. (1546-1696 (Electronic)).
25. Li B, Dewey CN. RSEM: accurate transcript quantification from RNA-Seq data with or without a reference genome. (1471-2105 (Electronic)).
26. Love Mi Fau - Huber W, Huber W Fau - Anders S, Anders S. Moderated estimation of fold change and dispersion for RNA-seq data with DESeq2. (1474-760X (Electronic)).
27. Wang L, Feng Z, Wang X, Wang X, Zhang X. DEGseq: an R package for identifying differentially expressed genes from RNA-seq data. *Bioinformatics*. 26(1):136-8.

28. Lu L, Wang JR, Henderson YC, Bai S, Yang J, Hu M, et al. Anaplastic transformation in thyroid cancer revealed by single-cell transcriptomics. *J Clin Invest.* 2023;133(11).
29. Chou TC. Theoretical basis, experimental design, and computerized simulation of synergism and antagonism in drug combination studies. *Pharmacol Rev.* 2006;58(3):621-81.
30. Chou TC, Talalay P. Quantitative analysis of dose-effect relationships: the combined effects of multiple drugs or enzyme inhibitors. *Adv Enzyme Regul.* 1984;22:27-55.
31. Chen S, Zhou Y, Chen Y, Gu J. fastp: an ultra-fast all-in-one FASTQ preprocessor. *Bioinformatics.* 2018;34(17):i884-i90.
32. Kim D, Langmead B, Salzberg SL. HISAT: a fast spliced aligner with low memory requirements. *Nat Methods.* 2015;12(4):357-60.
33. Pertea M, Pertea GM, Antonescu CM, Chang TC, Mendell JT, Salzberg SL. StringTie enables improved reconstruction of a transcriptome from RNA-seq reads. *Nat Biotechnol.* 2015;33(3):290-5.
34. Li B, Dewey CN. RSEM: accurate transcript quantification from RNA-Seq data with or without a reference genome. *BMC Bioinformatics.* 2011;12:323.
35. Love MI, Huber W, Anders S. Moderated estimation of fold change and dispersion for RNA-seq data with DESeq2. *Genome Biol.* 2014;15(12):550.
36. Wang L, Feng Z, Wang X, Wang X, Zhang X. DEGseq: an R package for identifying differentially expressed genes from RNA-seq data. *Bioinformatics.* 2010;26(1):136-8.
37. Jin Y, Van Nostrand D, Cheng L, Liu M, Chen L. Radioiodine refractory differentiated thyroid cancer. *Crit Rev Oncol Hematol.* 2018;125:111-20.
38. Sun M, Guo X, Qian X, Wang H, Yang C, Brinkman KL, et al. Activation of the ATM-Snail pathway promotes breast cancer metastasis. *J Mol Cell Biol.* 2012;4(5):304-15.
39. Subhash VV, Tan SH, Yeo MS, Yan FL, Peethala PC, Liem N, et al. ATM Expression Predicts Veliparib and Irinotecan Sensitivity in Gastric Cancer by Mediating P53-Independent Regulation of Cell Cycle and Apoptosis. *Mol Cancer Ther.* 2016;15(12):3087-96.
40. Liu X, Hu M, Liu P, Jiao M, Zhou M, Lee AK, et al. ATM Paradoxically Promotes Oncogenic Transformation via Transcriptional Reprogramming. *Cancer Res.* 2020;80(8):1669-80.
41. Shen M, Xu Z, Xu W, Jiang K, Zhang F, Ding Q, et al. Inhibition of ATM reverses EMT and decreases metastatic potential of cisplatin-resistant lung cancer cells through JAK/STAT3/PD-L1 pathway. *J Exp Clin Cancer Res.* 2019;38(1):149.
42. Nikjoo H, O'Neill P, Terrissol M, Goodhead DT. Quantitative modelling of DNA damage using Monte Carlo track structure method. *Radiat Environ Biophys.* 1999;38(1):31-8.
43. Sutherland BM, Bennett PV, Sidorkina O, Laval J. Clustered DNA damages induced in isolated DNA and in human cells by low doses of ionizing radiation. *Proc Natl Acad Sci U S A.* 2000;97(1):103-8.

44. Prabhu KS, Kuttikrishnan S, Ahmad N, Habeeba U, Mariyam Z, Suleman M, et al. H2AX: A key player in DNA damage response and a promising target for cancer therapy. *Biomed Pharmacother.* 2024;175:116663.
45. Yan S, Sorrell M, Berman Z. Functional interplay between ATM/ATR-mediated DNA damage response and DNA repair pathways in oxidative stress. *Cell Mol Life Sci.* 2014;71(20):3951-67.
46. Guo Z, Kozlov S, Lavin MF, Person MD, Paull TT. ATM activation by oxidative stress. *Science.* 2010;330(6003):517-21.
47. Das BB, Antony S, Gupta S, Dexheimer TS, Redon CE, Garfield S, et al. Optimal function of the DNA repair enzyme TDP1 requires its phosphorylation by ATM and/or DNA-PK. *EMBO J.* 2009;28(23):3667-80.
48. Cadet J, Wagner JR. DNA base damage by reactive oxygen species, oxidizing agents, and UV radiation. *Cold Spring Harb Perspect Biol.* 2013;5(2).
49. Fortini P, Dogliotti E. Base damage and single-strand break repair: mechanisms and functional significance of short- and long-patch repair subpathways. *DNA Repair (Amst).* 2007;6(4):398-409.
50. Mehnert JM, Varga A, Brose MS, Aggarwal RR, Lin CC, Prawira A, et al. Safety and antitumor activity of the anti-PD-1 antibody pembrolizumab in patients with advanced, PD-L1-positive papillary or follicular thyroid cancer. *BMC Cancer.* 2019;19(1):196.

Fig.1 Single-cell transcriptomic analysis identifies ATM upregulation

during thyroid cancer dedifferentiation. (A). Single-cell UMAP projection annotated with major cell types in thyroid tumors and normal tissues, with cell types distinguished by color. (B). A dot plot demonstrates the expression of key marker genes in different cell clusters. (C). Pseudotime trajectory analysis of transcriptional progression from normal thyroid follicular cells to malignant subtypes. (D). KEGG (Kyoto Encyclopedia of Genes and Genomes) pathway enrichment of differential genes (DEG) between the NORM and anaplastic thyroid cancers (ATC) groups along pseudotemporal trajectories. (E). Heatmap of cell cycle-related gene expression from normal thyroid follicular cells to malignant subtypes. (F). Scatter plots of key gene expression in the cell cycle and DNA replication regulation along the pseudotime in anaplastic

transformation in thyroid cancer.

Fig.2 ATM protein is overexpressed in advanced and radioiodine-refractory thyroid cancer. (A). Comparison of ATM H scores in the paraneoplastic tissue with the thyroid cancer (TC). (B). Comparison of ATM H scores in PTC, FTC, and ATC. The data are presented as mean \pm SD. * $P < 0.05$, **** $P < 0.0001$. Histogram distributions representing ATM expression in TC (C) and ATM expression in metastatic lymph nodes (D) in PTC (blue solid bar) and RAI-R PTC (red solid bar). The hashed black line represents the median ATM expression (tumor) in normal thyroid tissue, the hashed blue line represents the median ATM expression (tumor and metastatic lymph nodes) in the PTC, and the hashed red line represents the median ATM expression (tumor and metastatic lymph nodes) in the RAI-R PTC. (E). Correlation between *ATM* and *BRAF*, *KRAS*, *MTOR*, and *PIK3CA* expression levels in thyroid cancer TIMER (Tumor Immune Estimation Resource) dataset. Spearman's ρ value and p values are given. (F) Immunohistochemical (IHC) staining for ATM in normal thyroid tissue as well as in thyroid cancer, parathyroid tissue, and metastatic lymph nodes from thyroid cancer in PTC and RAI-R PTC. ATM, ataxia telangiectasia mutated; PTC, papillary thyroid cancer; FTC, follicular thyroid cancer; ATC, anaplastic thyroid cancer; RAI-R PTC, radioactive iodine refractory PTC; ATC, anaplastic thyroid cancer. Figure 2C and Figure 2D has been corrected to fix an axis label misplacement; no

change in data or statistical analysis.

Fig3. Pharmacological ATM inhibition synergizes with RAI to suppress tumor growth in vivo. (A). Mice were treated as shown in the scheme. Mice were randomized into four groups (n=7): Vehicle (i.p. injection of 100 μ L saline), RAI (a single i.p. injection of 37 MBq 131 I), iATM (i.p. injection of 5 mg/kg AZD1390 daily for 12 days), and RAI + iATM (a single i.p. injection of 37 MBq 131 I combined with daily i.p. 5 mg/kg AZD1390 for 12 days). (B-D). Tumor volume and tumor weight of different treatment groups. At the end of the experiment, intact tumors were removed for analysis. Tumor sections were stained with H&E, Ki-67, TUNEL, and γ H2AX. Statistical graphs and representative images are shown (D and E) (n = 7 in each group). TUNEL and IHC staining were performed on tumors harvested 24 hours after the final treatment. (F). Evaluation of liver and renal function following treatment. Serum levels of alanine aminotransferase (ALT), aspartate aminotransferase (AST), alkaline phosphatase (ALP), blood urea nitrogen (BUN), and creatinine (CR) were measured in each group. The data are presented as mean \pm SD. Ns, not significant, *P < 0.05, **P < 0.01, ***P < 0.001, and ****P < 0.0001.

Fig4. Genetic and pharmacological ATM blockade potentiates RAI-induced cytotoxicity and suppresses migration in vitro. (A). Viability of K1 cells treated with increasing activities of 131 I (0-55.5 MBq/mL) for 48 and

96 hours, assessed by CCK-8 assay (n=3). (B). Viability of K1 cells treated with increasing concentrations of AZD1390 (0-1200 nM) for 48 and 96 hours (n=3). (C). Viability of K1 cells treated with ^{131}I (2.3 MBq/mL) and increasing concentrations of AZD1390 (0-1200 nM) for 48 hours (n=3). (D). Combination effect of ^{131}I with AZD1390. (Combination index, CI, CI value > 1, Antagonism, CI value < 1, Synergism). (E). Clonal formation images and statistical results (F) of varying concentrations of AZD1390 in combination with ^{131}I on the proliferation of K1 cells. Cells were treated with ^{131}I (2.3 MBq/mL) and/or AZD1390 (5, 10 nM) for 24 hours, then grown in drug-free medium for 7 days before staining. (G-H). Flow cytometric analysis and quantification of apoptosis in K1 cells treated with ^{131}I (2.3 or 4.6 MBq/mL) for 24 hours and stained immediately with Annexin V/PI (n=3). (I-J). Flow cytometric analysis and quantification of apoptosis in K1 cells treated with ^{131}I (2.3 MBq/mL) and/or AZD1390 (50 nM) for 24 hours and stained immediately (n=3). (K). Western blot analysis confirming ATM knockdown efficiency in K1 cells, shNC, non-targeting control K1 cells, shATM, ATM-knockdown K1 cells. (L). Representative images of wound-healing assay at 0, 24 hours in control and ATM-knockdown groups. (M). Quantification of migration rate at 24 hours (n=3). Data are presented as mean \pm SD. *P < 0.05, **P < 0.01, ***P < 0.001, and ****P < 0.0001.

Fig5. RAI induces a base excision repair transcriptomic signature and

genotoxic stress without extensive double-strand breaks. (A). GO enrichment analysis for differentially expressed genes (DEGs) between non-RAI and RAI-treated (4.6 MBq/mL, 72 hours) K1 cells (FDR < 0.05). (B). GSEA of DEGs between the same groups. (C). Heatmap showing DEGs associated with the DNA damage response pathway in the non-RAI and RAI groups. Heatmap colors indicate normalized gene expression from high (red) to low (blue). (D, K). EdU proliferation assay and quantification of K1 cells after ^{131}I (4.6 MBq/mL) treatment for 48h. Edu proportion ratio = (%Edu-positive area) / (%DAPI-positive area). (E, K). TUNEL staining and quantification 48 hours after ^{131}I (4.6 MBq/mL) exposure or DNase I treatment. TUNEL proportion ratio = (% tunel-positive area) / (% DAPI-positive area). (F, I, K). Representative images and quantification of double-stranded DNA (dsDNA) and nuclear DNA (DAPI) in K1 cells 24 hours after stimulation with ^{131}I (4.6 MBq/mL) or cisplatin. (G, K). Comet assay after ^{131}I (4.6 MBq/mL) exposure or DNase I treatment for 24h of K1 cells, and quantitative and statistical analysis (K) of the alkaline tail moment (n = 50 in each group). (H, J, K). Representative images and quantification of single-stranded DNA (ssDNA) and nuclear DNA (DAPI) in K1 cells 24 hours after ^{131}I (4.6 MBq/mL) stimulation For immunofluorescence panels (D, E, F, H), n=3. The data are presented as mean \pm SD. *P < 0.05, **P < 0.01, and ****P < 0.0001, ns, no significance.

Fig6. ATM inhibition abrogates the G2/M checkpoint and exacerbates

RAI-induced genotoxic stress. (A, B, D). Flow cytometric analysis and quantification of the cell cycle in K1 cells 24 hours after treatment with the indicated activities of ^{131}I . (C, E). Flow cytometric analysis and quantification of the cell cycle in K1 cells treated with ^{131}I (2.3 MBq/mL) and/or AZD1390 (50 nM) for 24 hours. (F, G). Western blot images and quantitative analysis of phospho-CDC2, phospho-CHK2, ATM, and phospho-ATM protein expression in K1 cells after 24-hour treatment with AZD1390 (50 nM) or ^{131}I (2.3 MBq/mL), alone and in combination. (H). Cell viability of K1 cells following treatments with ^{131}I (4.6 MBq/mL) for 24 hours, after which the medium was replaced with fresh medium or medium containing AZD1390 (50 nM) for the indicated durations and number of AP sites following treatments ($n = 3$). The data are presented as mean \pm SD. * $P < 0.05$, ** $P < 0.01$, *** $P < 0.001$, and **** $P < 0.0001$.

Supplement figure legends

Fig.S1 Quality control and extended analysis of single-cell RNA sequencing data. (A). Cell proportions per sample. 9 of the 15 ATC samples that met the quality control standards were included in the analyses. (B). Cell annotation of normal thyroid tissues and malignant subtypes. (C). Pseudotime trajectory of transcriptional progression from normal thyroid follicular cells to malignant subtypes. (D). Heatmap showing the dynamic changes of gene expression along pseudotime. The differentially expressed genes were clustered hierarchically into three groups, and the representative enriched

pathways of each group were shown.

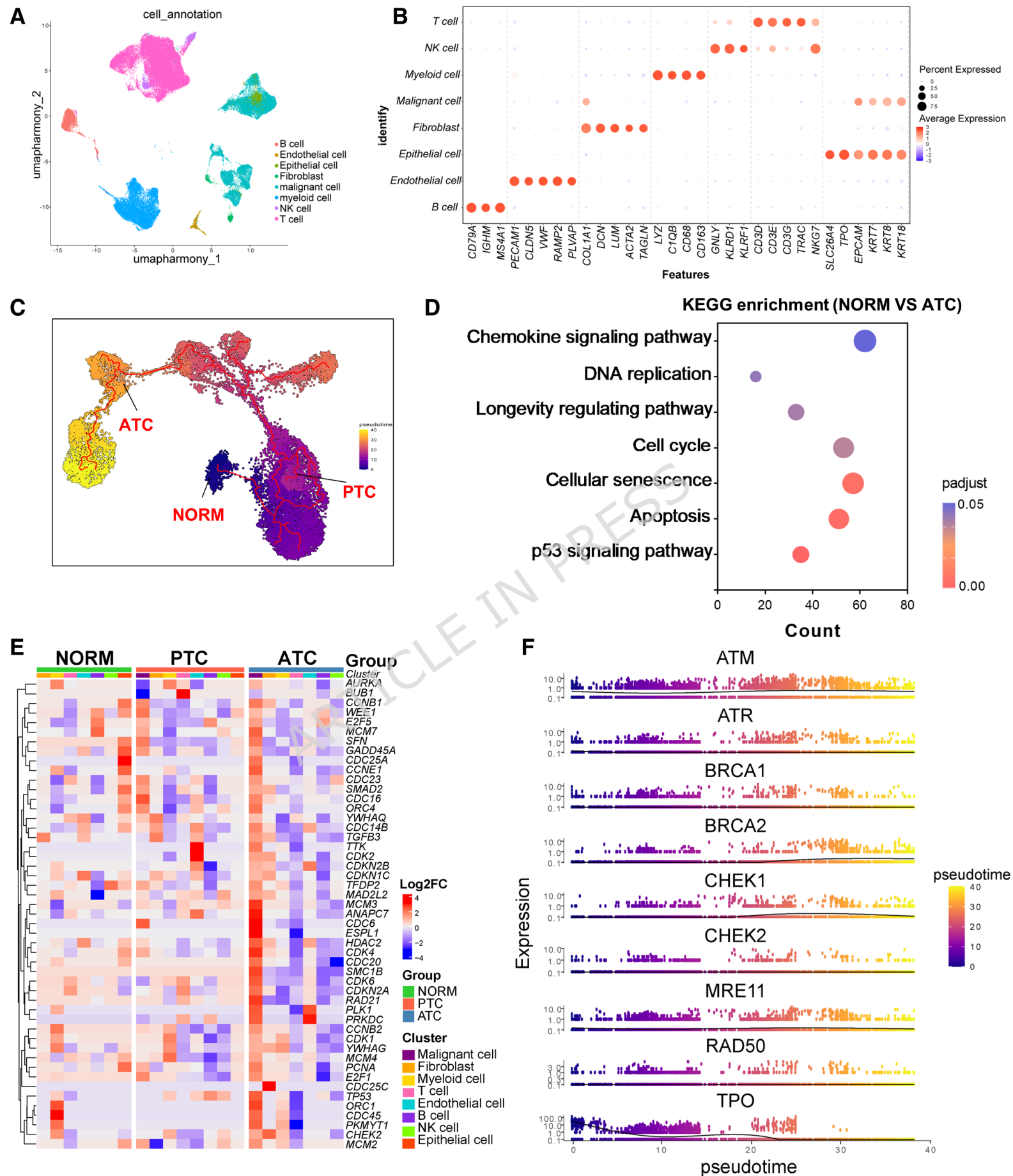
Fig.S2 Composition and annotation of the thyroid cancer tissue microarray. (A). Panoramic scan of tissue microarray. (B). This diagram uses the color code and symbols denote the different tissue origins of the samples analyzed in Fig. S2A.

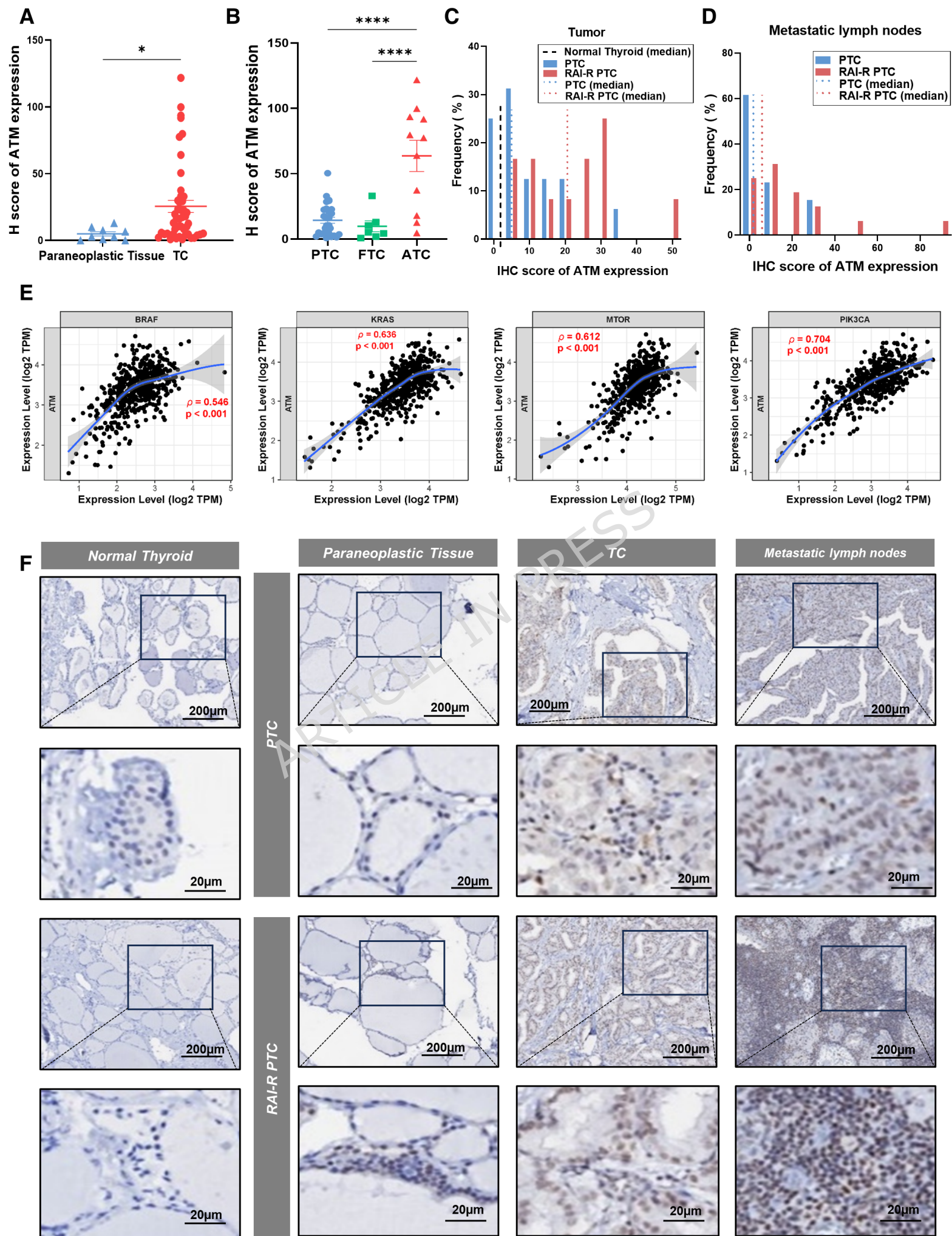
Fig.S3 Characterization of thyroid cancer cell lines and validation of AZD1390 on RAI uptake. (A). Intracellular ^{131}I accumulation was measured using γ counter in different thyroid cancer cell lines. (B). Quantitative PCR (qPCR) analysis of *ATM* mRNA expression in a panel of differentiated thyroid cancer cell lines (K1, BCPAP, TPC-1). (C). K1 cells were treated with AZD1390 (6h and 12h) or vehicle control, and intracellular ^{131}I accumulation was measured using γ counter. (n = 3 in each group). The data are presented as mean \pm SD. Ns, not significant, **P < 0.01, and ***P < 0.001.

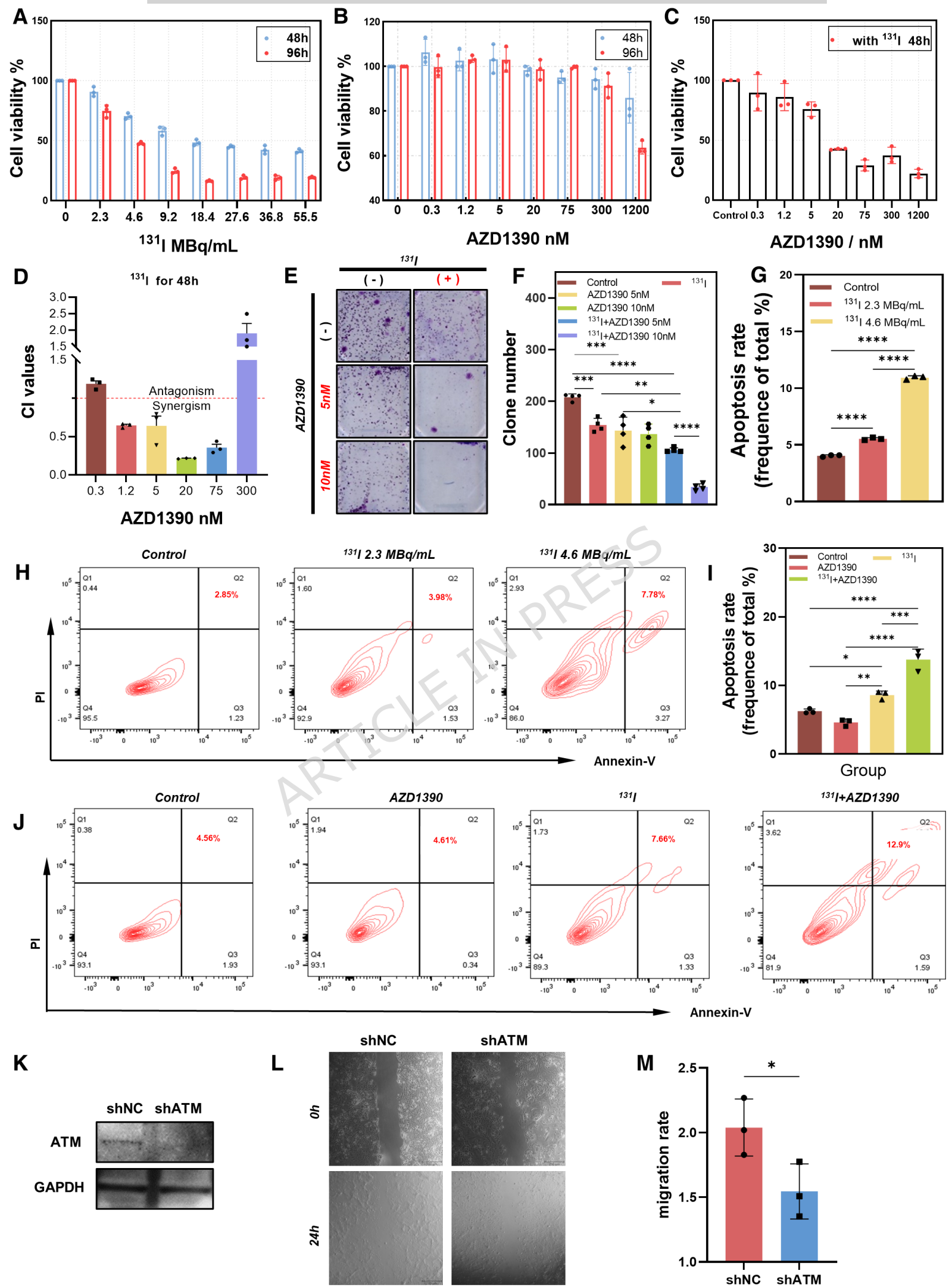
Fig. S4 Genetic knockdown of ATM enhances RAI-induced apoptosis. (A-B). Flow cytometric analysis and quantification of apoptosis in shNC K1 cells or shATM K1 cells treated with ^{131}I (2.3 MBq/mL) for 24 hours and stained immediately, shNC, non-targeting control K1 cells, shATM, ATM-knockdown K1 cells (n=3). Data are presented as mean \pm SD. **P < 0.01, ***P < 0.001, and ****P < 0.0001.

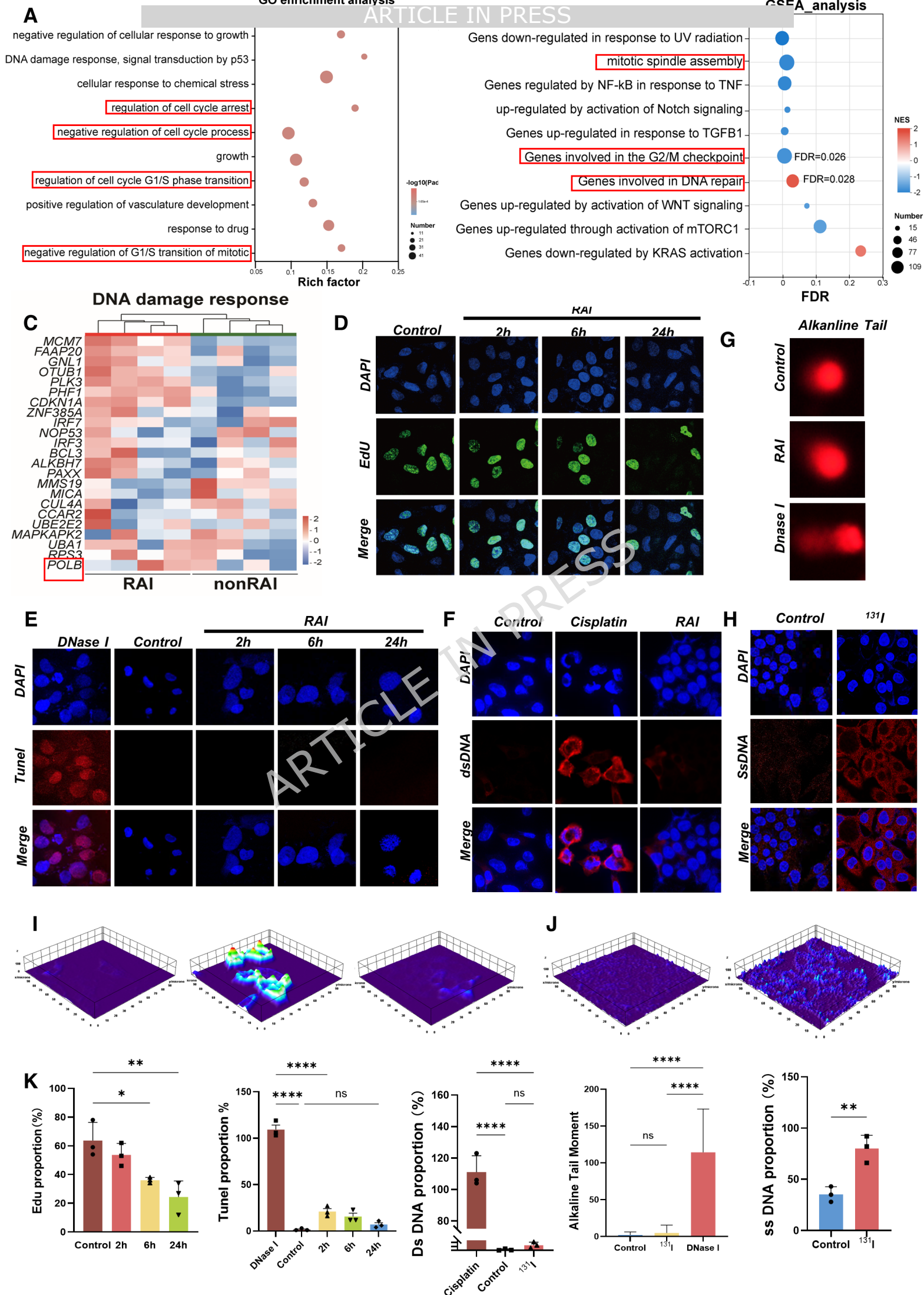
Fig.S5 Transcriptomic profiling of K1 cells in response to RAI treatment. (A). Volcano plot showing the differentially expressed genes (DEGs) in the non-RAI and RAI groups. (B). KEGG enrichment analysis for upregulating DEGs ($p < 0.05$).

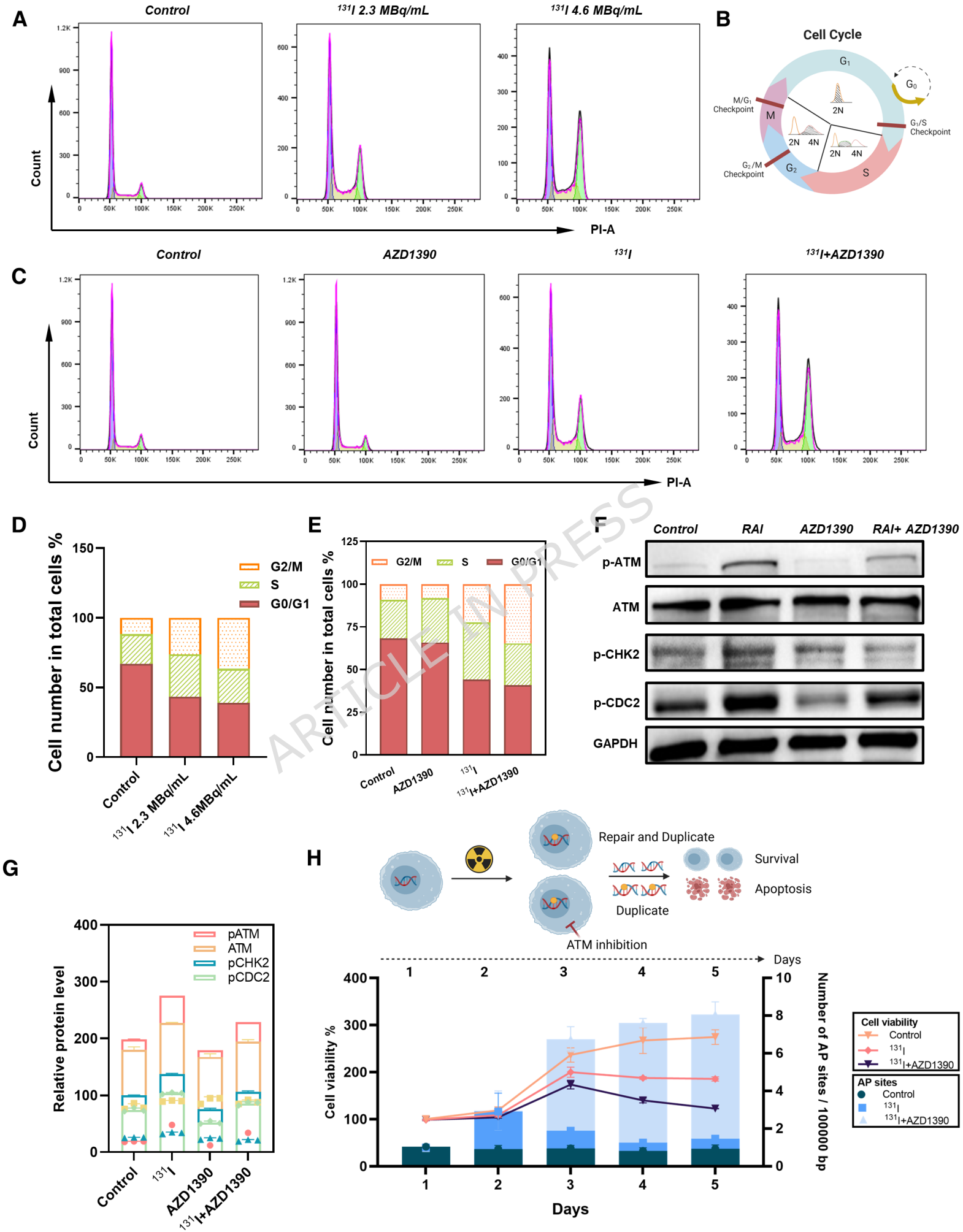
Fig.S6 Western blot analysis for phospho-CDC2. (A-B). Western blot images and quantitative analysis of phospho-CDC-2 expression after treatment of K1 cells with AZD1390, ^{131}I (4.8 MBq/mL) alone, or a combination of ^{131}I -AZD1390 for 24 hours.

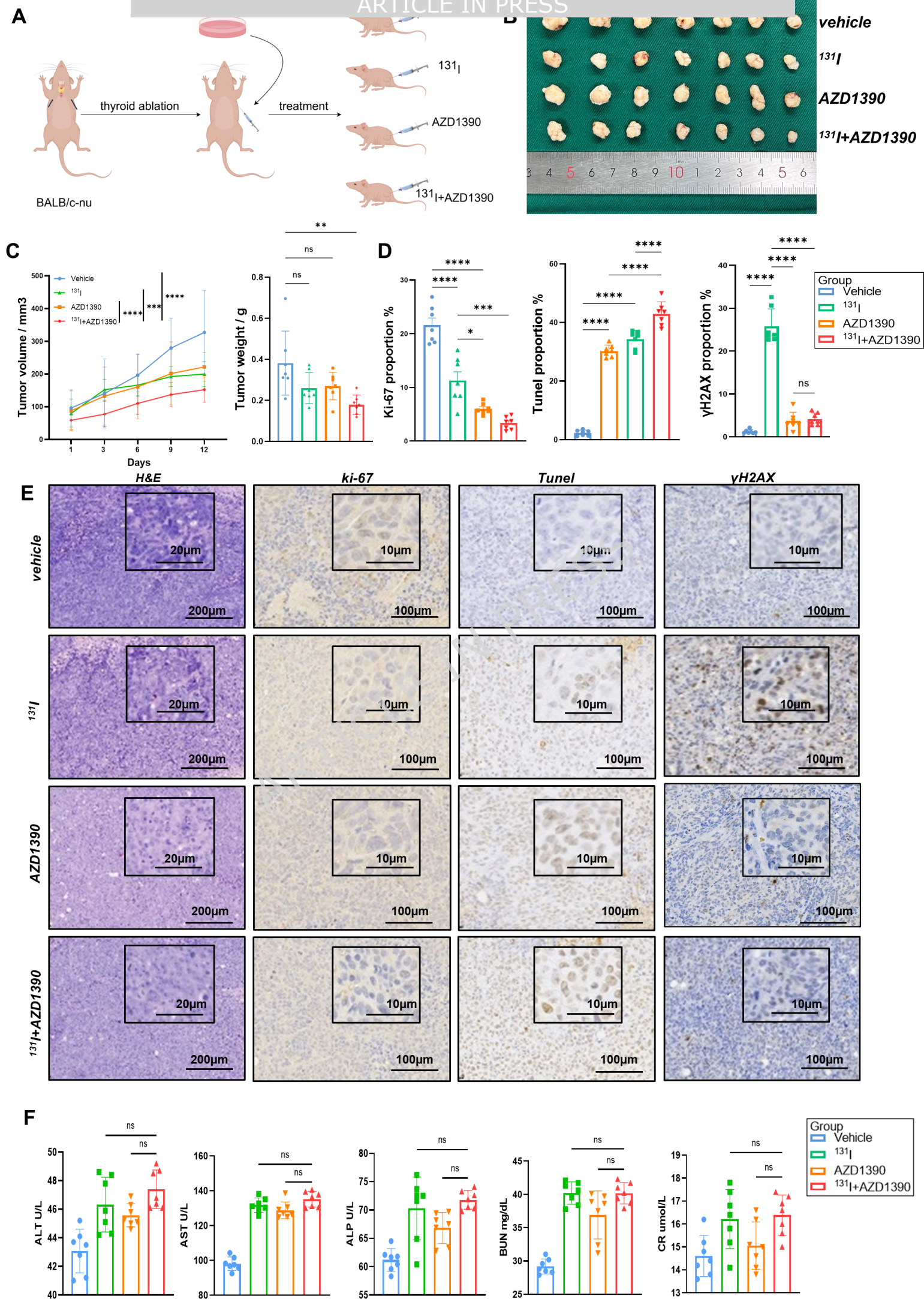












Sample IDs	Tissue Origins	Cancer type	Patient IDs	Age	Sex	T	N
TFC01	Normal thyroid	Nodular goiter	TFC01	22	F	/	/
TFC02	Normal thyroid	Nodular goiter	TFC02	67	M	/	/
TFC03	Normal thyroid	Nodular goiter	TFC03	54	F	/	/
TFC04	Normal thyroid	Nodular goiter	TFC04	60	F	/	/
TFC05	Normal thyroid	Nodular goiter	TFC05	30	F	/	/
TFC06	Normal thyroid	Nodular goiter	TFC06	45	F	/	/

M	Treatment	Radioactive iodine-refractory	BRAF mutatio	RAS mutatio	TERT promote	RET mutatio
/	untreated	na	na	na	na	na
/	untreated	na	na	na	na	na
/	untreated	na	na	na	na	na
/	untreated	na	na	na	na	na
/	untreated	na	na	na	na	na
/	untreated	na	na	na	na	na

ARTICLE IN PRESS

Sample IDs	Tissue Origins	Cancer type	Patient IDs	Age	Sex	T	N	M
PTC01	PTC	tumcdifferenti	PTC01	36	M	T1a	N1b	M0
PTC02	PTC	tumcdifferenti	PTC02	39	F	T1b	N1b	M0
PTC03	PTC	tumcdifferenti	PTC03	25	F	T2	N1b	M0
PTC04	PTC	tumcdifferenti	PTC04	67	F	T1a	N0	M0
PTC05	PTC	tumcdifferenti	PTC05	33	F	T4a	N1b	M0
PTC06	PTC	tumcdifferenti	PTC06	17	F	T1b	N1b	M0
PTC07	PTC	tumcdifferenti	PTC07	33	F	T3	N1b	M0
PTC08	PTC	tumcdifferenti	PTC08	20	F	T3a	N1b	M0
PTC09	PTC	tumcdifferenti	PTC09	36	M	T4a	N1b	M0
PTC10	PTC	tumcdifferenti	PTC10	84	F	T1b	N1b	M0
PTC11	PTC	tumcdifferenti	PTC11	36	F	T1a	N1a	M0
PTC12	PTC	tumcdifferenti	PTC12	34	F	T1b	N1a	M0
PTC13	PTC	tumcdifferenti	PTC13	45	F	T2	N1b	M0
PTC14	FTC	tumcfollicular	PTC14	72	F	T3a	N0	M0
PTC15	PTC	tumcdifferenti	PTC15	50	F	T2	N0	M0
PTC16	PTC	tumcdifferenti	PTC16	63	F	T2	N1a	M0

ARTICLE IN PRESS

Treatment	Radioactive	BRAF mutation	RAS mutation	TERT promote	RET mutation
untreated	na	mut	wt	wt	na
untreated	na	mut	wt	wt	na
untreated	na	mut	wt	wt	na
untreated	na	mut	wt	wt	na
untreated	na	mut	wt	wt	na
untreated	na	mut	wt	wt	na
untreated	na	mut	wt	wt	na
untreated	na	mut	wt	wt	na
untreated	na	mut	wt	wt	na
untreated	na	mut	wt	mut	na
untreated	na	mut	wt	wt	wt
untreated	na	mut	wt	wt	na
untreated	na	wt	wt	wt	mut
untreated	na	wt	mut	wt	wt
untreated	na	wt	wt	wt	wt
untreated	na	mut	wt	mut	na

ARTICLE IN PRESS

Sample IDs	Tissue Origins	Cancer type	Patient IDs	Age	Sex	T	N	M
RAIR-PTC	PTC	tumcdifferenti	RAIR-PTC	33	M	T1b	N0	M0
RAIR-PTC	PTC	tumcdifferenti	RAIR-PTC	56	F	T3	N1b	M0
RAIR-PTC	PTC	tumcdifferenti	RAIR-PTC	32	M	T1b	N1b	M0
RAIR-PTC	PTC	tumcdifferenti	RAIR-PTC	33	M	T3	N1b	M0
RAIR-PTC	PTC	tumcdifferenti	RAIR-PTC	35	F	T2	N1b	M0
RAIR-PTC	PTC	tumcdifferenti	RAIR-PTC	26	F	T1b	N1a	M0
RAIR-PTC	PTC	tumcdifferenti	RAIR-PTC	50	F	T1a	N1a	M0
RAIR-PTC	PTC	tumcdifferenti	RAIR-PTC	68	F	T3b	N1a	M0
RAIR-PTC	PTC	tumcdifferenti	RAIR-PTC	55	F	T2	N1b	M0
RAIR-PTC	PTC	tumcdifferenti	RAIR-PTC	22	M	T1b	N1a	M0
RAIR-PTC	PTC	tumcdifferenti	RAIR-PTC	48	F	T4	N1b	M0
RAIR-PTC	PTC	tumcdifferenti	RAIR-PTC	53	F	T4a	N1a	M0

ARTICLE IN PRESS

Treatment	Radioactive	BRAF mutation	RAS mutation	TERT promote	RET mutation
untreated	yes	wt	na	wt	na
untreated	yes	mut	wt	wt	na
untreated	yes	mut	na	wt	na
untreated	yes	mut	na	wt	na
untreated	yes	mut	na	na	na
untreated	yes	mut	na	wt	na
untreated	yes	mut	na	na	na
untreated	yes	mut	na	wt	na
untreated	yes	mut	na	wt	na
untreated	yes	mut	na	wt	na
untreated	yes	mut	wt	wt	na
untreated	yes	mut	wt	wt	na

Sample IDs	Tissue Origins	Cancer type	Patient IDs	Age	Sex	T	N	M
FTC01	FTC tumcfollicular	FTC01	46 F	T2	Nx	M0		
FTC02	FTC tumcfollicular	FTC02	49 F	T4b	N1a	M0		
FTC03	FTC tumcfollicular	FTC03	74 F	T1a	Nx	M0		
FTC04	FTC tumcfollicular	FTC04	47 F	T4b	N0	M0		
FTC05	FTC tumcfollicular	FTC05	50 M	T1b	N0	M0		
FTC06	FTC tumcfollicular	FTC06	35 M	T4b	Nx	M0		
FTC07	FTC tumcfollicular	FTC07	33 F	T2	N0	M0		

Treatment	Radioactive	BRAF mutation	RAS mutation	TERT promote	RET mutation
untreated	na	wt	na	wt	wt
untreated	na	na	na	na	na
untreated	na	na	na	na	na
untreated	na	wt	na	na	na
untreated	na	wt	na	na	na
untreated	na	wt	wt	wt	wt
untreated	na	na	na	na	na

Sample IDs	Tissue Origins	Cancer type	Patient IDs	Age	Sex	T	N	M
ATC01	ATC tum	canaplasti	ATC01	66	M	T1b	N1b	M0
ATC02	ATC tum	canaplasti	ATC02	60	F	T1a	N0	M0
ATC03	ATC tum	canaplasti	ATC03	65	F	T3b	N1b	M0
ATC04	ATC tum	canaplasti	ATC04	54	M	T2	N1a	M0
ATC05	ATC tum	canaplasti	ATC05	73	F	T3a	N0	M0
ATC06	ATC tum	canaplasti	ATC06	82	F	T4b	N0	M0
ATC07	ATC tum	canaplasti	ATC07	56	M	T2	N1b	M0
ATC08	ATC tum	canaplasti	ATC08	77	F	T3a	N1a	M0
ATC09	ATC tum	canaplasti	ATC09	59	F	T4b	N0	M0
ATC10	ATC tum	canaplasti	ATC10	28	F	T4b	N1a	M0
ATC11	ATC tum	canaplasti	ATC11	71	F	T2	Nx	M0

ARTICLE IN PRESS

Treatment	Radioactive	BRAF mutation	RAS mutation	TERT promote	RET mutation
untreated	na	na	na	na	na
untreated	na	na	na	na	na
untreated	na	mut	na	wt	na
untreated	na	na	na	na	na
untreated	na	na	na	na	na
untreated	na	wt	na	wt	na
untreated	na	na	na	na	na
untreated	na	na	na	na	na
untreated	na	na	na	na	na
untreated	na	na	na	na	na
untreated	na	wt	na	wt	wt

Sample IDs	Tissue Origins	Cancer type	Patient IDs	Age	Sex	T	N	M
Paraneop	Paraneop	differenti	PTC01	36	M	T1a	N1b	M0
Paraneop	Paraneop	differenti	PTC02	39	F	T1b	N1b	M0
Paraneop	Paraneop	differenti	PTC03	25	F	T2	N1b	M0
Paraneop	Paraneop	differenti	PTC04	67	F	T1a	N0	M0
Paraneop	Paraneop	differenti	PTC05	33	F	T4a	N1b	M0
Paraneop	Paraneop	differenti	PTC06	17	F	T1b	N1b	M0
Paraneop	Paraneop	differenti	PTC07	33	F	T3	N1b	M0
Paraneop	Paraneop	differenti	PTC08	20	F	T3a	N1b	M0
Paraneop	Paraneop	differenti	PTC09	36	M	T4a	N1b	M0

[illegible]

Sample IDs	Tissue Origins	Cancer type	Patient IDs	Age	Sex	T	N	M
PTC-LN01	PTC	tumcdifferenti	PTC02	39	F	T1b	N1b	M0
PTC-LN02	PTC	tumcdifferenti	PTC03	25	F	T2	N1b	M0
PTC-LN03	PTC	tumcdifferenti	PTC04	67	F	T1a	N0	M0
PTC-LN04	PTC	tumcdifferenti	PTC05	33	F	T4a	N1b	M0
PTC-LN05	PTC	tumcdifferenti	PTC06	17	F	T1b	N1b	M0
PTC-LN06	PTC	tumcdifferenti	PTC07	33	F	T3	N1b	M0
PTC-LN07	PTC	tumcdifferenti	PTC08	20	F	T3a	N1b	M0
PTC-LN08	PTC	tumcdifferenti	PTC09	36	M	T4a	N1b	M0
PTC-LN09	PTC	tumcdifferenti	PTC10	84	F	T1b	N1b	M0
PTC-LN10	PTC	tumcdifferenti	PTC11	36	F	T1a	N1a	M0
PTC-LN11	PTC	tumcdifferenti	PTC12	34	F	T1b	N1a	M0
PTC-LN12	PTC	tumcdifferenti	PTC13	45	F	T2	N1b	M0
PTC-LN13	PTC	tumcdifferenti	PTC14	72	F	T3a	N0	M0

Treatment	Radioactive	BRAF mutation	RAS mutation	TERT promote	RET mutation
untreated	na	mut	wt	wt	na
untreated	na	mut	wt	wt	na
untreated	na	mut	wt	wt	na
untreated	na	mut	wt	wt	na
untreated	na	mut	wt	wt	na
untreated	na	mut	wt	wt	na
untreated	na	mut	wt	wt	na
untreated	na	mut	wt	wt	na
untreated	na	mut	wt	mut	na
untreated	na	mut	wt	wt	wt
untreated	na	mut	wt	wt	na
untreated	na	wt	wt	wt	mut
untreated	na	wt	mut	wt	wt

Sample IDs	Tissue Origins	Cancer type	Patient IDs	Age	Sex	T	N	M
RAI-R PT(PTC metadifferenti	RAI-R PT(PTC metadifferenti	RAI-R PT(PTC metadifferenti	RAI-R PT(PTC metadifferenti	59	M	T1a	N1a	M0
RAI-R PT(PTC metadifferenti	RAI-R PT(PTC metadifferenti	RAI-R PT(PTC metadifferenti	RAI-R PT(PTC metadifferenti	63	F	T1a	N1a	M0
RAI-R PT(PTC metadifferenti	RAI-R PT(PTC metadifferenti	RAI-R PT(PTC metadifferenti	RAI-R PT(PTC metadifferenti	62	F	T2	N1a	M0
RAI-R PT(PTC metadifferenti	RAI-R PT(PTC metadifferenti	RAI-R PT(PTC metadifferenti	RAI-R PT(PTC metadifferenti	29	F	T2	N1b	M0
RAI-R PT(PTC metadifferenti	RAI-R PT(PTC metadifferenti	RAI-R PT(PTC metadifferenti	RAI-R PT(PTC metadifferenti	63	M	T1b	N1a	M0
RAI-R PT(PTC metadifferenti	RAI-R PT(PTC metadifferenti	RAI-R PT(PTC metadifferenti	RAI-R PT(PTC metadifferenti	10	F	T2	N1b	M0
RAI-R PT(PTC metadifferenti	RAI-R PT(PTC metadifferenti	RAI-R PT(PTC metadifferenti	RAI-R PT(PTC metadifferenti	46	F	T1a	N1a	M0
RAI-R PT(PTC metadifferenti	RAI-R PT(PTC metadifferenti	RAI-R PT(PTC metadifferenti	RAI-R PT(PTC metadifferenti	28	F	T1b	N1b	M0
RAI-R PT(PTC metadifferenti	RAI-R PT(PTC metadifferenti	RAI-R PT(PTC metadifferenti	RAI-R PT(PTC metadifferenti	31	F	T2	N1a	M0
RAI-R PT(PTC metadifferenti	RAI-R PT(PTC metadifferenti	RAI-R PT(PTC metadifferenti	RAI-R PT(PTC metadifferenti	57	F	T2	N1a	M0
RAI-R PT(PTC metadifferenti	RAI-R PT(PTC metadifferenti	RAI-R PT(PTC metadifferenti	RAI-R PT(PTC metadifferenti	25	F	T1b	N1a	M0
RAI-R PT(PTC metadifferenti	RAI-R PT(PTC metadifferenti	RAI-R PT(PTC metadifferenti	RAI-R PT(PTC metadifferenti	34	M	T1b	N1b	M0
RAI-R PT(PTC metadifferenti	RAI-R PT(PTC metadifferenti	RAI-R PT(PTC metadifferenti	RAI-R PT(PTC metadifferenti	39	F	T1b	N1b	M0
RAI-R PT(PTC metadifferenti	RAI-R PT(PTC metadifferenti	RAI-R PT(PTC metadifferenti	RAI-R PT(PTC metadifferenti	50	F	T1a	N1a	M0
RAI-R PT(PTC metadifferenti	RAI-R PT(PTC metadifferenti	RAI-R PT(PTC metadifferenti	RAI-R PT(PTC metadifferenti	53	F	T4a	N1a	M0

ARTICLE IN PRESS

Treatment	Radioactive	BRAF mutation	RAS mutation	TERT promote	RET mutation
One rad	yes	mut	na	na	na
One rad	yes	mut	na	na	na
One rad	yes	mut	na	mut	na
One rad	yes	mut	na	wt	na
One rad	yes	mut	na	wt	na
One rad	yes	wt	na	wt	na
One rad	yes	na	na	na	na
One rad	yes	mut	na	wt	na
One rad	yes	mut	na	na	na
One rad	yes	mut	na	na	na
One rad	yes	mut	na	wt	na
One rad	yes	mut	na	na	na
One rad	yes	mut	wt	wt	na
One rad	yes	mut	wt	wt	na
One rad	yes	mut	wt	wt	na

ARTICLE IN PRESS